Article

Molecular basis for selective activation of DREADD-based chemogenetics

https://doi.org/10.1038/s41586-022-05489-0

Received: 30 June 2022

Accepted: 27 October 2022

Published onli ne: 30 November 2022

Check for updates

Shicheng Zhang[1,4], Ryan H. Gumpper[1,4], Xi-Ping Huang[1,2], Yongfeng Liu[1,2], Brian E. Krumm[1], Can Cao[1], Jonathan F. Fay[3]✉ & Bryan L. Roth[1]✉

Designer receptors exclusively activated by designer drugs (DREADDs) represent a powerful chemogenetic technology for the remote control of neuronal activity and cellular signalling[1–4]. The muscarinic receptor-based DREADDs are the most widely used chemogenetic tools in neuroscience research. The G_q-coupled DREADD (hM3Dq) is used to enhance neuronal activity, whereas the $G_{i/o}$-coupled DREADD (hM4Di) is utilized to inhibit neuronal activity[5]. Here we report four DREADD-related cryogenic electron microscopy high-resolution structures: a hM3Dq–miniG_q complex and a hM4Di–miniG_o complex bound to deschloroclozapine; a hM3Dq–miniG_q complex bound to clozapine-*N*-oxide; and a hM3R–miniG_q complex bound to iperoxo. Complemented with mutagenesis, functional and computational simulation data, our structures reveal key details of the recognition of DREADD chemogenetic actuators and the molecular basis for activation. These findings should accelerate the structure-guided discovery of next-generation chemogenetic tools.

Chemogenetic[1–4] and optogenetic[6] technologies are widely used for the remote control of neuronal and non-neuronal activity and signalling. DREADDs, the most widely used chemogenetic technology in neuroscience, were first developed through directed molecular evolution in yeast of human muscarinic acetylcholine receptors (mAChRs)[5]. Such DREADDs display minimal basal activity, are insensitive to the endogenous ligand acetylcholine (ACh) and are activated by the pharmacologically inert designer drug clozapine-*N*-oxide (CNO)[5] (Fig. 1a,b). DREADDs based on muscarinic receptors (M1R–M5R) were generated by introducing two site-specific mutations, Y3x33C and A5x461G (generic residue number in the GPCRdb[7]) on the mAChRs[5]. Of these, the M1R, M3R and M5R DREADDs (hM1Dq, hM3Dq and hM5Dq, respectively) activate $G_{q/11}$ signalling, whereas the M2R and M4R DREADDs (hM2Di and hM4Di, respectively) activate $G_{i/o}$ signalling[5]. The G_q-coupled DREADD hM3Dq is most frequently used to enhance neuronal activity through G_q-mediated depolarization, Ca^{2+} mobilization and ion channel activity modulation. The $G_{i/o}$-coupled DREADD hM4Di is widely used to inhibit neuronal activity through Gβγ-mediated activation of hyperpolarizing GIRK channels and inhibition of the synaptic release of neurotransmitters (Fig. 1b). Furthermore, hM3Dq was used as a platform for engineering G_q and β-arrestin signalling-biased DREADDs[8,9] and G_s-coupled and G_{12}-coupled DREADDs ($M3D_s$ and $M3D_{12}$, respectively)[10,11].

CNO represents the most widely used chemogenetic actuator, even though it has been reported to be back-metabolized to clozapine (CLZ) in mice, rats, guinea pigs and humans[12–14]. As CLZ is an antipsychotic drug with high affinities for a large number of neurotransmitter receptors[15], such transformation can be accompanied by off-target actions in vivo. Moreover, CNO displays low brain penetrance after systemic drug injection[13]. To overcome these issues, new chemogenetic actuators have been developed, including compound 21 (C21), perlapine (PLP), olanzapine (OLP), JHU37152 (J52), JHU37160 (J60) and deschloroclozapine (DCZ)[16–20]. Of these, DCZ represents the newest chemogenetic actuator with the highest affinity, greatest selectivity and improved metabolic stability for the mAChR-based DREADDs[17].

Although DREADDs are ubiquitously used in neuroscience research, we lack an understanding of how these evolved receptors display such ligand specificity. In large measure, this is because the receptors were engineered before the structural elucidation of mAChRs. To understand the molecular mechanisms of ligand specificity and signalling, we determined three mAChR-based DREADD complexes: hM3Dq and hM4Di in complex with two chemogenetic actuators (DCZ and CNO). We also solved the wild-type (WT) human M3R (hM3R) in complex with the synthetic agonist iperoxo. On the basis of these structures and together with biochemical, signalling and molecular dynamics (MD) simulation studies, we report the molecular details responsible for chemogenetic actuator recognition by DREADDs and provide new insights into the agonist selectivity and activation of DREADDs. These structural insights into DREADD–ligand recognition should accelerate the discovery of more selective and potent chemogenetic actuators.

Structures of transducer-coupled DREADD complexes

For structural determination, the hM3Dq and hM4Di expression constructs were generated by introducing two site-specific mutations (Y3x33C and A5x461G) to WT hM3R and hM4R, respectively. To improve the yield and stability of the receptors, the intracellular loop 3 of both hM3Dq and hM4Di were partially removed (Extended Data Fig. 1a,b). Previously validated miniG_q (refs. [21,22]) and miniG_o (refs. [23,24]) proteins were used for the assembly of complexes with hM3Dq and hM4Di, respectively. Eventually, both the DCZ-bound complexes of hM3Dq–miniG_q–scFv16

[1]Department of Pharmacology, School of Medicine, University of North Carolina at Chapel Hill, Chapel Hill, NC, USA. [2]National Institute of Mental Health Psychoactive Drug Screening Program (NIMH PDSP), School of Medicine, University of North Carolina at Chapel Hill, Chapel Hill, NC, USA. [3]Department of Biochemistry and Molecular Biology, University of Maryland School of Medicine, Baltimore, MD, USA. [4]These authors contributed equally: Shicheng Zhang, Ryan H. Gumpper. ✉e-mail: jfay@som.umaryland.edu; bryan_roth@med.unc.edu

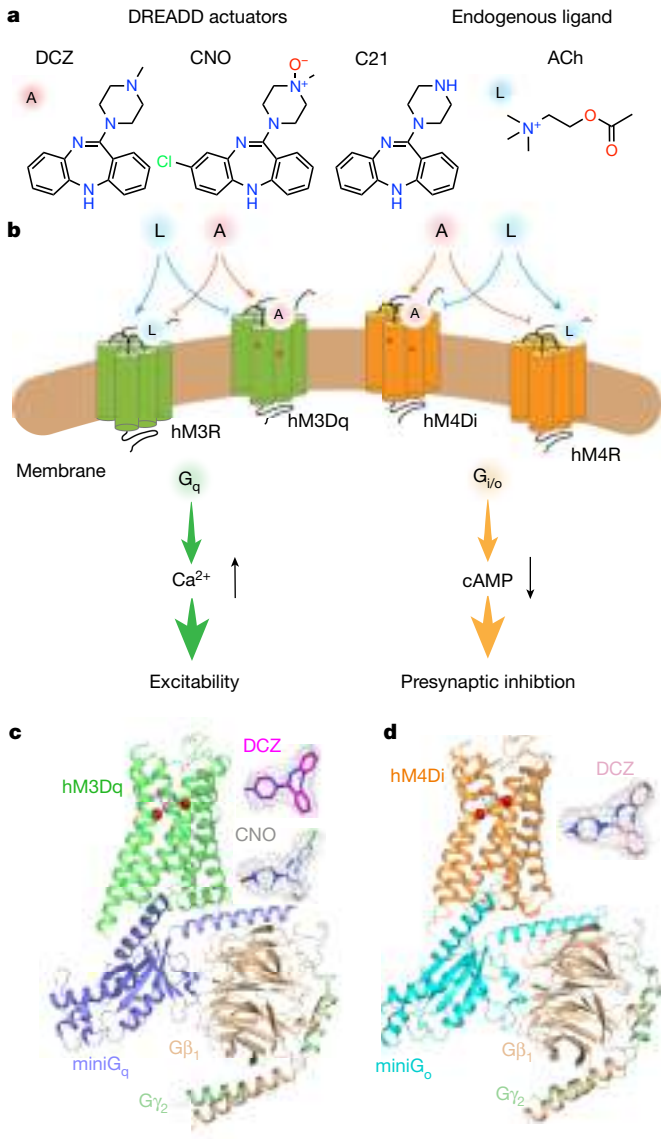

Fig. 1 | Overall structures of the DREADD complexes. a, Chemical structures of the DREADD actuators and endogenous ligand ACh. **b**, Schematic working model of the DREADD system. The A and L are short for the DREADD actuators and endogenous ligand, respectively. The red asterisks on the receptors indicate the DREADD mutations, Y3x33C and A5x461G (Y, tyrosine; C, cysteine; A, alanine; G, glycine; and the 3x33 and 5x461 are the generic residue numbers of these two DREADD residues in the GPCRdb). **c**,**d**. Overall structures of the DCZ-bound hM3Dq–miniG_q (**c**) and hM4Di–miniG_o complex (**d**), respectively. The Cα of DREADD mutations on the structures are shown in red spheres and the ligands are in the ball-and-stick model. Next to the structure models of the DREADD complexes, actuators (DCZ and CNO) are shown in stick models surrounded by electron microscopy maps shown in grey meshes.

and hM4Di–miniG_o–scFv16 were determined at overall nominal resolutions of 2.7 Å (Fig. 1c,d, Extended Data Fig. 2 and Extended Data Table 1). Because CNO has low affinity for hM3Dq and hM4Di, the NanoBit tethering system was used to obtain more stable complexes[24,25]. This strategy enabled the CNO-bound hM3Dq–miniG_q–scFv16 complex to be solved at a resolution of 2.8 Å (Fig. 1c, Extended Data Fig. 2 and Extended Data Table 1). In addition, the high structural similarity between CNO-bound (with NanoBit) and DCZ-bound (without NanoBit) hM3Dq–miniG_q–scFv16 complexes indicated that the NanoBit tethering system did not affect structural properties (Supplementary Fig. 1).

To gain insights into the difference between the DREADD and WT muscarinic receptor complexes, we determined the structure of an iperoxo-bound hM3R–miniG_o–scFv16 complex at a higher resolution of 2.55 Å than the previously reported hM1R–G_{11}, hM2R–G_{oA} and hM4R–G_i complexes[26,27] (Extended Data Fig. 2 and Extended Data Table 1). By applying local refinement on the receptor, we obtained an isolated, continuous and clear density map in the orthosteric binding pocket (OBP) of hM3R, and this high-quality map enabled us to unambiguously fit iperoxo in the binding pocket (Extended Data Fig. 3a). Notably, previously determined inactive structures of M3R are from the rat[28–30]; therefore, this study provides a previously unreported structure of hM3R. Of the 49 non-conserved residues, 6 residues are in the structured region. None of them are located at the ligand-binding pocket or at the receptor–G protein interface (Supplementary Fig. 2). A comparison of the overall structures between the DCZ-bound hM3Dq–miniG_q and iperoxo-bound hM3R–miniG_q complexes indicated high similarity, with root mean square deviation (RMSD) values of 0.57 Å for the entire complex and 0.48 Å for the receptor alone. This result suggests that the DREADD complex shares a similar mechanism for G protein signal transduction (Extended Data Fig. 3a).

Actuator recognition at DREADDs

The high-resolution structures of the transducer-coupled DREADD complexes enabled us to gain insights into the molecular recognition of the potent DREADD actuator DCZ and the widely used actuator CNO. As the binding poses of DCZ and the conformation of surrounding residues in both DREADD complexes were similar, DCZ-bound hM4Di was used to elucidate the recognition modality of DCZ (Fig. 2a). Overall, the recognition of DCZ at hM4Di is mainly based on its two chemical moieties: a piperazine ring and a tricyclic core (Fig. 2b). First, on the piperazine ring, the basic amino group forms a salt bridge interaction with $D112^{3x32}$, and the methyl group is buried into the hydrophobic pocket formed by $Y439^{7x38}$, $C442^{7x41}$ and $Y443^{7x42}$ (Fig. 2a). Second, the upper benzene ring of the tricyclic core occupies the extended binding pocket and has hydrophobic interactions with $W164^{4x57}$, $I187^{45x52}$, $F189^{ECL2}$ (in which ECL2 is extracellular loop 2), $L190^{ECL2}$, $T196^{5x40}$, $A200^{5x44}$ and $V420^{6x55}$ (Fig. 2b and Extended Data Fig. 4a). The middle diazepine ring forms two specific hydrogen bonds with $Y416^{6x51}$ and $N417^{6x52}$, whereas the lower benzene ring mainly interacts with $W164^{4xx57}$ and $W413^{6x48}$ through π–π interactions (Fig. 2a,b and Extended Data Fig. 4a). The recognition modality for CNO was similar to DCZ, except for the *N*-oxidate and 8-chloro group (Fig. 2e). Because of *N*-oxidation, the methyl group in CNO deflects to the transmembrane helix 6 (TM6) side, and the negatively charged oxygen atom takes the place of the *N*-methyl group in DCZ, accompanied by minor rotamer changes of the Y7x38 and Y7x42 residues (Fig. 2e). The 8-chloro group of CNO forms interactions with T5x40 and has hydrophobic contacts with V6x55 and $L226^{ECL2}$ (Extended Data Fig. 4b).

In the iperoxo-bound hM3R structure, the binding pose of iperoxo is almost identical to that in the iperoxo-bound hM1R–G_{11} and hM2R–G_{oA} structures (Extended Data Fig. 4c). However, some differences were observed, including the network of hydrogen bonds among the Y3x33, Y6x51, Y7x38 (termed the tyrosine lid), D3x32 and Y7x42 residues. As a result of the rotameric difference of Y7x38, this residue forms a hydrogen bond with D3x32 in the iperoxo–hM3R and DCZ-bound hM3Dq structures instead of interacting with Y3x33 as in the active hM1R and hM2R structures (Fig. 2c,d and Extended Data Fig. 4c). A comparison of the binding pockets between iperoxo and DCZ revealed an extra and deeper subpocket occupied by the heterocyclic group of iperoxo (Extended Data Fig. 4d). Moreover, unlike the fully embedded binding pocket of iperoxo, the pocket that DCZ occupied is bigger and opens a narrow channel to the extracellular region in the DREADD complex (Fig. 2f,g).

Functional role of key residues in the binding pocket

To evaluate the functional role of the surrounding residues in the binding pocket, we performed mutagenesis studies of both hM4Di

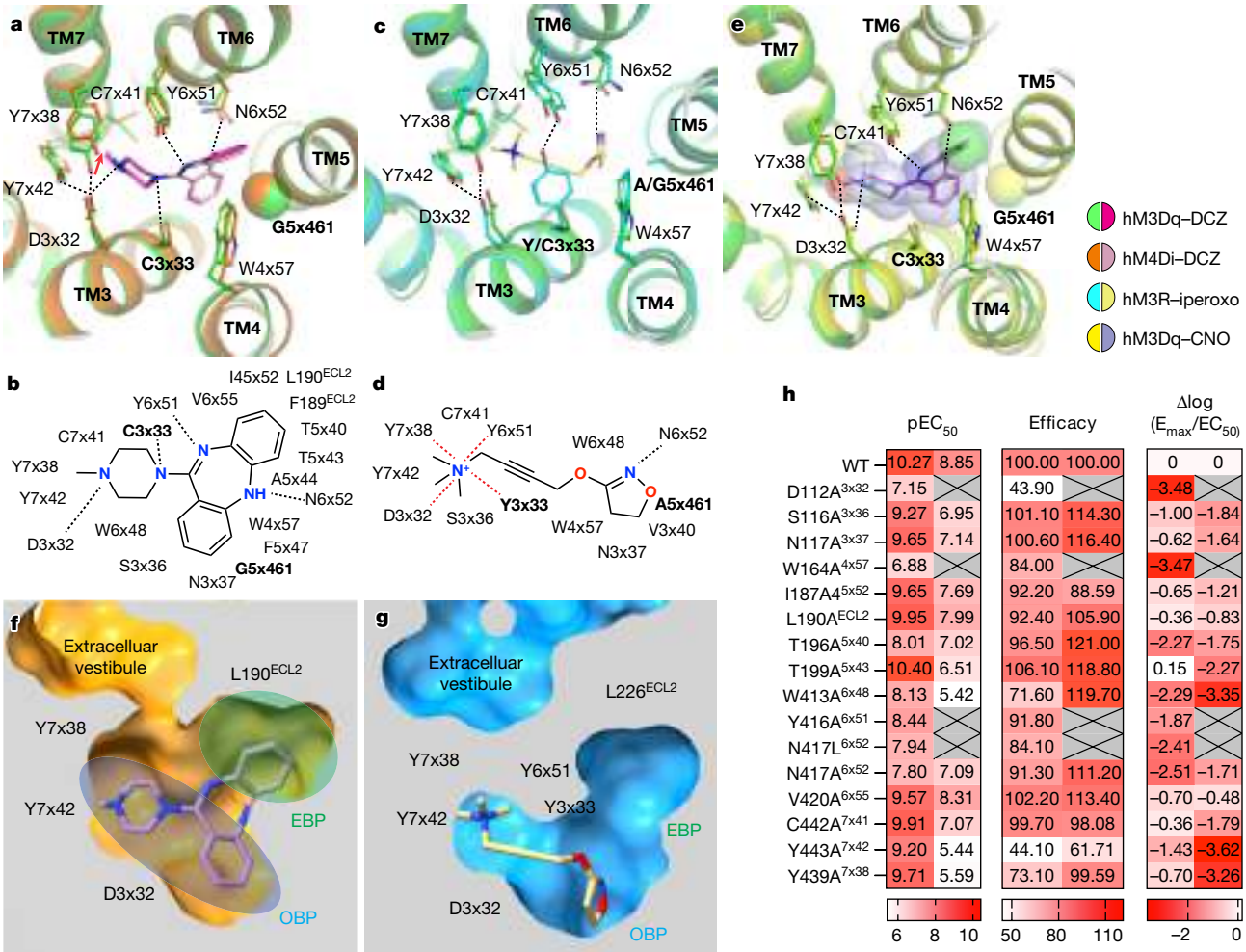

Fig. 2 | Actuator recognition at DREADDs. a, Close-up view of binding pockets of the hM3Dq–DCZ structure superposed with the hM4Di–DCZ structure. Both DCZs and related residues are shown in stick models except the Cα of G5x461 in the sphere. The hydrogen bonds in the hM3Dq–DCZ structure are shown as black dashed lines. The rotamer difference of Y7x38 from hM3Dq to hM4Di is indicated by a red arrow. **b**, 2D diagram of the interactions between hM4Di and DCZ. **c**, Close-up view of binding pockets of the hM3R–iperoxo structure (locally refined) superposed with the hM3Dq–DCZ structure. Both the iperoxo and surrounding residues are shown in the ball-and-stick model. The hydrogen bonds in the hM3R–iperoxo structure are shown as black dashed lines. **d**, 2D diagram of the interactions between hM3R and iperoxo. Specific hydrogen bonds are shown as black dashed lines in **b** and **d**. The salt bridge and π–cation interactions are indicated by red dashed lines. **e**, Close-up view of the binding pockets of hM3Dq–CNO superposed with hM3Dq–DCZ. Ligands CNO and DCZ and related residues are shown in stick models except the Cα of G5x461 in the sphere. The hydrogen bonds in the hM3Dq–CNO structure are shown as black dashed lines. Specifically, two DREADD residues Y/C3x33 and A/G5x461 are labelled in bold in **a**–**e**. **f**,**g**, Cut views of the binding pockets of hM4Di–DCZ (**f**) and hM3R–iperoxo (**g**) structures. The OBP and extended binding pocket (EBP) are indicated by the blue and green-shaded ovals, respectively. **h**, Heatmap of the mutagenesis studies showing the effects of residues in the binding pockets of hM4R or hM4Di by the BRET2 G_{oA}-activation assay stimulated by ACh or DCZ, respectively, in HEK293T cells. Boxes marked with X indicate 'not detected' as no appreciable signal was detected. See Supplementary Fig. 3 for the fitted curves and Supplementary Table 1 for the detailed parameter values. EC_{50}, half maximal effective concentration; E_{max}, maximal response; pEC_{50}, negative log EC_{50}.

and hM4R and tested the mutants using bioluminescence resonance energy transfer (BRET) assays. We also calculated transduction coefficients to incorporate the effects of mutations on both potency and efficacy[31]. The results indicated that most mutants of hM4R affected the ACh-induced activation of G_{oA} signalling (Fig. 2h and Supplementary Fig. 3). The following observations were made: (1) the mutants D112^{3x32}A, W164^{4x57}A and Y416^{6x51}A lost the ability to activate G_{oA} signalling; (2) T199^{5x43}A, W413^{6x38}A, Y439^{7x38}A and Y443^{7x42}A severely affected signalling; (3) S116^{3x36}A, N117^{3x37}A, I187^{ECL2}A, T196^{5x40}A, N417^{6x52}A and C442^{7x41}A substantially reduced signalling; and (4) only L190^{ECL2}A and V420^{6x55}A showed modest effects on G_{oA} signalling (Fig. 2h). By contrast, hM4Di mutants displayed fewer effects on G_{oA} signalling activation following DCZ stimulation. Specifically, none of the mutants abolished activity, whereas D112^{3x32}A, W164^{4x57}A, T196^{5x40}A, W413^{6x38}A and N417^{6x52}A greatly attenuated activity. In addition, S116^{3x36}A, Y416^{6x51}A and Y443^{7x42}A displayed moderate effects on the activation of G_{oA} signalling (Fig. 2h). Notably, the surface expression levels of D112^{3x32}A, Y416^{6x51}A and Y443^{7x42}A of hM4R were significantly lower than the WT receptor (less than 50%) (Supplementary Fig. 4a). This result indicates that these three strictly conserved residues also play crucial parts in the stability of hM4R (Supplementary Fig. 5).

Significantly, alanine substitution of any member of the tyrosine lid network had large effects on the ACh-stimulated activation of hM4R and moderate effects on DCZ-stimulated hM4Di activation (Figs. 2h and 3a). Specifically, Y416^{6x51} has a hydrogen bond with DCZ, and the Y-to-A mutation had greater effects on the activation of the DREADD than the Y439^{7x38}A mutation (Fig. 2a,h). In addition, although N6x52 forms a hydrogen bond with both DCZ and iperoxo, the mutation N417^{6x52}A displayed a more extreme effect in receptor activation for hM4Di than for hM4R (Fig. 2a,c,h). The mutation N417^{6x52}L had a similar effect to that of

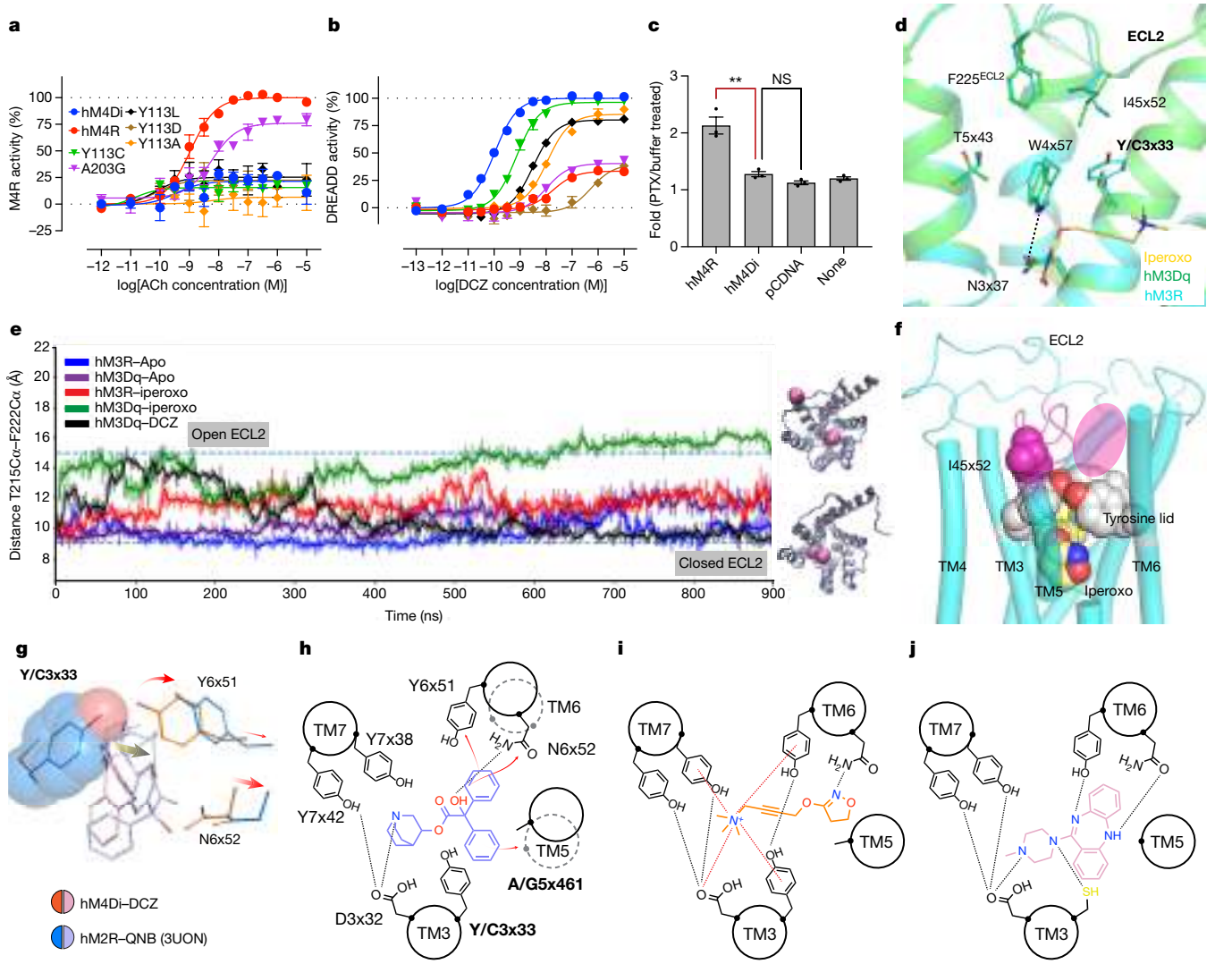

Fig. 3 | Insights into the selective activation of DREADDs. a,**b**, BRET2 G_{oA}-activation of hM4R, hM4Di and their mutants stimulated by ACh (**a**) and DCZ (**b**) in HEK293T cells, respectively. See Supplementary Table 2 for fitted parameter values that represent the mean ± s.e.m. of $n = 3$ biologically independent experiments. **c**, Basal activities of hM4R and hM4Di determined by cAMP assays in HEK293T cells. Data represent the mean ± s.e.m. The significant difference ($n = 3$, $P = 0.0054$, unpaired two-tailed Student's t-test) between hM4R and hM4Di is indicated by $^{**}P < 0.01$. NS, not significant. **d**, Interaction networks mediated by W4x57, including the hydrophobic cluster formed with Y/C3x33, T5x43, I45x52 and $F225^{ECL2}$ and hydrogen bonding with N3x37. **e**, MD simulations of ECL2 conformations. Plots of averaged simulations ($N = 3$) of the distance are measured from T215 Cα to F222 Cα. The representative open and closed conformational models (Cα of T215 and F222 are shown in spheres) are shown on the right. **f**, Diagrammatic summary of the roles of Y3x33 in recognizing and stabilizing iperoxo. Residues Y3x33, Y6x51, Y7x38 (tyrosine lid), I45x52 and iperoxo are shown in grey, magenta and pale yellow spheres, respectively. The ECL2 region between C45x50 and I5x39 (hM3R) is in magenta. The binding site for the positive allosteric modulator LY2033298 is indicated by a magenta-shaded oval. **g**, Interactions between DCZ or QNB and Y/C3x33, Y6x51 and N6x52 in the hM4Di or the hM2R structure. The Y3x33 residue is shown in spheres. The conformational changes of the ligands and residues are indicated by grey and red arrows, respectively. **h**,**j**, Schematic diagrams of the interactions between ligands and WT or DREADD receptors in antagonist mode (**h**), agonist mode (**i**) and DREADD mode (**j**). The hydrogen bonds and electrostatic interactions are indicated as black and red dashed lines, respectively. The interactions potentially inducing the transmembrane movements are indicated by red arrows in **h**. DREADD residues Y/C3x33 and A/G5x461 are labelled in bold in **d**,**g**,**h**.

$N417^{6x52}A$, both of which severely affected the function of hM4Di (Fig. 2h). Thus, these two hydrophilic interactions between the actuator and TM6 are vital for the activation of the DREADD. Notably, a strictly conserved residue, $T199^{5x43}$, across the mAChR family had distinct roles in the signalling activation of hM4R and hM4Di (Fig. 2h and Supplementary Fig. 5). The tested mutant severely affected the activation of hM4R but had almost no effects on the activation of hM4Di (Fig. 2h). Several previous studies have also shown that the mutant T5x43A alters the binding affinities and potencies of most agonists without altering antagonist affinities[32,33]. However, although there is no direct interaction between T5x43 and iperoxo, it forms hydrophobic interactions with W4x57 and $F225^{ECL2}$. This interaction might have important roles in the iperoxo-induced activation of WT receptors; this possibility is considered below (Fig. 3d). All the pocket residues were strictly conserved across the mAChR family. The only exception was Phe in hM2R instead of Leu as for the other mAChRs at the third position following 45x52 (Supplementary Fig. 4).

Insights into the agonist selectivity of DREADDs

A feature of the DREADD system is insensitivity to endogenous ligands. For the muscarinic receptor-based DREADDs, ACh is relatively inactive[5,34,35]. Here we report that the ACh-like synthetic agonist iperoxo also loses binding affinities and displayed greatly attenuated agonist activities towards DREADDs (Extended Data Fig. 5a–h). As in previous

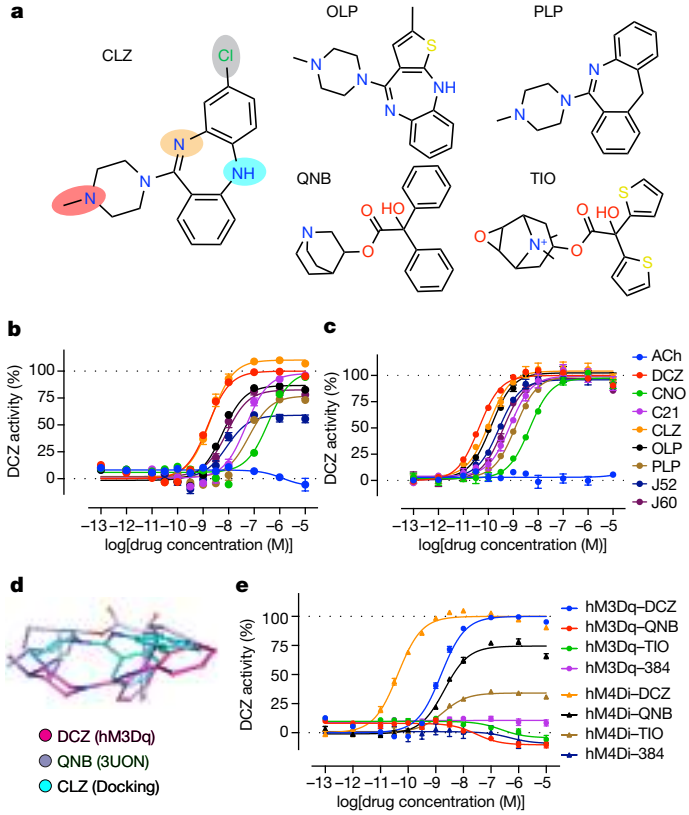

Fig. 4 | Comparison of the DREADD actuators. a, Chemical structures of CLZ, OLP, PLP, QNB and TIO. Specific recognition elements identified from the DCZ and CNO-bound DREADD structures are indicated by magenta, yellow, blue, and grey ovals. **b**,**c**, Activities of the DREADD actuators towards hM3Dq (**b**) and hM4Di (**c**) by BRET2 G_q- and G_{oA}-activation assays, respectively, in HEK293T cells. See Supplementary Table 3 for fitted parameter values that represent the mean ± s.e.m. of $n = 3$ biologically independent experiments. **d**, Top view of the structural superposition of the DCZ (in the hM3Dq structure), QNB (in the hM2R structure; Protein Data Bank (PDB) identifier: 3UON) and CLZ (docked in the inactive state rM3R structure; PDB identifier: 4DAJ). **e**, Activities of QNB, TIO and AF-DX384 (384) towards hM3Dq and hM4Di by BRET2 G_q- and G_{oA}-activation assays, respectively, in HEK293T cells. See Supplementary Table 3 for fitted parameter values that represent the mean ± s.e.m. of $n = 3$ biologically independent experiments.

studies[5], the Y3x33C mutation abolished ACh-induced activation, whereas A5x461G produced a mutant receptor with lower ACh potency and efficacy (Fig. 3a). As described above, the primary role of Y3x33 is in the formation of the conserved tyrosine lid with Y6x51 and Y7x38. This not only forms π–cation interactions with the positive charge of iperoxo or ACh but also directly covers the OBP to stabilize ACh or its analogues (Fig. 2c,g). Thus, the DREADD mutation Y3x33C directly loses this π–cation interaction with the ACh-like agonists and results in a much more open OBP, which in turn leads to the attenuation of binding affinities (Fig. 2c,f,g and Extended Data Fig. 5a–d). Docking iperoxo into the OBPs of the hM3R and hM3Dq structures demonstrated that in contrast to the relatively stable binding poses in hM3R, the binding poses in hM3Dq are more flexible. That is, the terminal ring (4,5-dihydroisoxazole) of iperoxo in hM3Dq is flipped up and down with comparable docking scores for each pose (Supplementary Fig. 6a,b).

To further clarify the differences in the binding pockets between the WT receptors and DREADDs, MD simulations were performed using the iperoxo-bound hM3R structure and the hM3Dq structure with a docked iperoxo molecule (Supplementary Videos 1 and 2). From these simulations, a second potential role for Y3x33 was revealed. This residue is also involved in the interaction network with W4x57, I45x52, $F225^{ECL2}$, T5x43 and N3x37 in the hM3R structure (Fig. 3d). This network not only stabilized the conformation of Y3x33 and W4x57 but also bridged the interaction between the tyrosine lid and ECL2. However, this network was weakened in DREADDs by the Y3x33C substitution. In the iperoxo–hM3R simulation, the W4x57–N3x37 interaction was unstable, and the side chain of N3x37 rotated freely and formed a hydrogen bond with the flipped heterocyclic ring of iperoxo (Extended Data Fig. 6d,h,i and Supplementary Video 1). By contrast, in the iperoxo–hM3Dq simulation, as the strong edge-to-face π–π stacking interaction between Y3x33 and W4x57 is absent, the W4x57–N3x37 interaction was more stable and thus locked the rotamer of N3x37, which made N3x37 unable to form hydrogen bonds with iperoxo (Extended Data Fig. 6e,j,k and Supplementary Video 2).

In addition, an effect of Y3x33C on the dynamics of ECL2 was also observed (Fig. 3e, Supplementary Fig. 7 and Supplementary Videos 3 and 4). In the simulations of hM3R–Apo and hM3Dq–DCZ, the ECL2 molecules were stable (termed 'close' confirmation). For hM3R–iperoxo and hM3Dq–Apo, the ECL2 molecules were moderately dynamic, and for hM3Dq–iperoxo, the ECL2 was highly dynamic (termed 'open' conformation) (Fig. 3e). As mentioned above, Y3x33C weakens the interactions with W4x57, I45x52 and $F225^{ECL2}$, which leads to a relatively dynamic conformation of ECL2 in comparison with the WT receptor (Fig. 3d). Meanwhile, in the hM3Dq–DCZ structure, instead of Y3x33, the upper benzene ring of DCZ interacted with ECL2 residues and thus stabilized its conformation (Extended Data Fig. 4a,b). The ECL2, especially the region from I5x39 of TM5 to the conserved C45x50 residue, is located on the top of the tyrosine lid and affects the binding of ACh-like agonists (Fig. 3f). This notion is also supported by an analysis of the binding sites of several positive allosteric modulators, such as LY2119620 in hM2R and hM4R[26,27,34,35]. They stabilize the conformation of ECL2 by binding to the space among ECL2, TM6 and TM7 to enhance ACh-like agonist-induced receptor activation (Fig. 3f). Together, these findings suggest that two features (ECL2 and the tyrosine lid) located on the top of the OBP could stabilize the binding of ACh-like agonists to the pocket and therefore enhance receptor activation (Fig. 3f). The instability of any layer therefore affects the binding of ACh-like agonists, which consequently affects receptor activation. Notably, residue Y3x33 has key roles in both layers and in agonist recognition. These findings could also explain why residues such as N3x37, W4x57, I45x57 and T5x43, which are not directly engaged in the interaction with iperoxo, have large effects on the ACh-induced activation of hM4R (Fig. 2c, and h).

Finally, the mutation A5x461G also reduced the ACh-induced or iperoxo-induced activation of hM4R (Fig. 3a and Extended Data Fig. 6a). This result implicated a role for A5x461G in the selective activation of DREADDs, albeit with less importance than Y3x33C. In the hM3R–iperoxo structure, A5x461 exhibited hydrophobic interactions with the heterocyclic ring (Fig. 2c,d and Extended Data Fig. 4d), which might contribute to the stabilization of iperoxo in the binding pocket. This finding was supported by further MD simulations using an iperoxo-bound hM3R (A5x461G) structure, which showed that the heterocyclic ring of iperoxo was highly unstable and swung extensively in the binding pocket (Extended Data Fig. 6f,l,m and Supplementary Video 5).

Molecular mechanisms of DREADD activation

The other key feature of the DREADD system is the large gain of agonist functionality by chemogenetic actuators (Fig. 1b). To gain insights into the molecular mechanisms of DREADD activation, we first investigated the antagonism of mAChRs by comparing DCZ-bound DREADD structures and antagonist-bound mAChR structures[29,30,36] (Fig. 3g and Extended Data Fig. 4e–g). Similar conformation changes in the overall structure were observed in the following two pairs of comparisons: hM3Dq–DCZ and tiotropium-bound rat M3R (rM3R–TIO)[29], and hM4Di–DCZ and 3-quinuclidinyl benzilate-bound hM2R

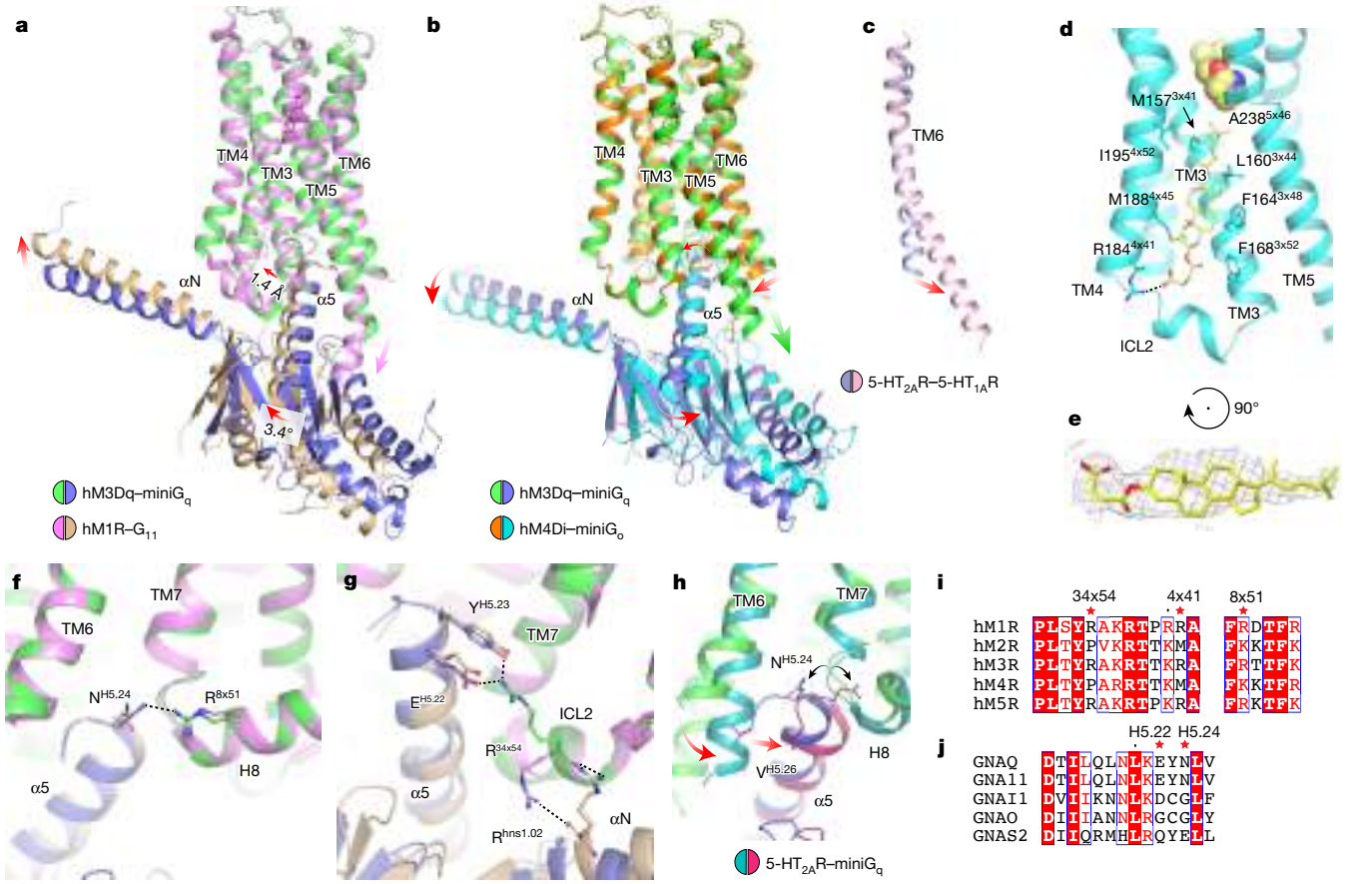

Fig. 5 | Subtype determinators for muscarinic receptors. a, Superposition of the hM3Dq–miniG$_q$ and hM1R–G$_{11}$ (PDB identifier: 6OIJ) complexes. The helical extension of TM5 of hM1R is indicated by a pink arrow. Conformational differences of αN and α5 of G proteins and ICL2 of receptors from hM3Dq–miniG$_q$ to hM1R–G$_{11}$ are indicated by red arrows. Specifically, the rotation of α5 is measured on the basis of each Cα of R$^{H5.05}$ to the Cα of Y$^{H5.23}$, and the ICL2 shift is measured on the basis of Cα of L34x51. **b**, Superposition of the hM3Dq–miniG$_q$ and hM4Di–miniG$_o$ complexes. The rotation of the α5 helix and shift of the αN helix of miniG$_o$ in comparison with miniG$_q$ are indicated by red arrows. The extension of TM5 of hM3Dq and the inward movement of TM6 of hM4Di are indicated by a green and red arrow, respectively. **c**, Superposition of the TM6 of 5-HT$_{2A}$R (PDB identifier: 6WHA) and 5-HT$_{1A}$R (PDB identifier: 7E2Y). **d**, CHS binding site in hM3R–iperoxo (locally refined) structure. The ligand iperoxo is presented in spheres. The CHS molecule and surrounding residues are shown in the stick model. The salt bridge interaction between CHS and R184 is indicated by a blank dashed line. **e**, Electron microscopy map for the CHS molecule is shown as grey meshes. **f**,**g**, Comparison of the receptor–G protein interfaces mediated by N$^{H5.24}$ (**f**) and E$^{H5.22}$ (**g**) between hM3Dq–miniG$_q$ and hM1R–G$_{11}$ complex, respectively. Hydrogen bonds are indicated by black dashed lines. **h**, Comparison of G$_{q/11}$ binding modes in hM3Dq and 5-HT$_{2A}$R (PDB identifier: 6WHA). **i**,**j**, Sequence alignments of the mAChR family (**i**) and Gα subunits (**j**). Strictly conserved residues are highlighted in filled red boxes and conserved residues are in open red boxes. Specifically, three arginines (R^{34x54}, R^{4x41}, and R^{8x51}) of G$_q$-coupled subtype mAChRs and two residues (E$^{H5.22}$ and N$^{H5.24}$) of the G$_{q/11}$ family are indicated by asterisks in **i** and **j**, respectively.

(hM2R–QNB)[36]. Specifically, compared with the DREADD complex, TM6 of the antagonist-bound structure displayed an outward displacement accompanied by a tilt of TM5 towards the TM6 side at the extracellular side (Extended Data Fig. 4e,f). Furthermore, we compared the binding poses of the ligands and conformational changes of the surrounding residues in the binding pocket between DCZ and TIO or QNB (Fig. 3g and Extended Data Fig. 4g). To accommodate the side chain of Y3x33, the two ring moieties of TIO and QNB displayed slight downward movements, with the upper rings displaced to the TM5–TM6 side. Subsequently, TM6 was pushed outward through direct interactions between the ester and hydroxyl groups of TIO and QNB and N6x52. Meanwhile, Y6x51 was also displaced outward along with the TM6 movement and lost the interaction with Y3x33 (Fig. 3g and Extended Data Fig. 4g). Collectively, Y3x33 and N6x52 have important roles in the antagonism of QNB and TIO (Fig. 3h).

In the iperoxo-bound hM3R–miniG$_q$ structure, the interaction network formed through the tyrosine lid (Y3x33, Y6x51 and Y7x38), D3x32 and Y7x42 bridged the connections between TM3, TM6 and TM7. By contrast, these connections were disrupted in DREADDs as the Y3x33 is substituted by a cysteine residue. As there are no structures of apo WT mAChRs reported yet, we performed a structural comparison of iperoxo-bound hM3R with the predicted structure of hM3R from the Alphafold2 server[37]. The result indicated an almost identical interaction network of these five residues (Extended Data Fig. 4h). Thus, we assumed that this network has potential roles in maintaining the basal activity of these receptors. This hypothesis is supported by measurements of basal activities using a cAMP Glo-sensor assay for hM4Di and additional BRET2 assays for both hM3Dq and hM4Di (Fig. 3c and Extended Data Fig. 6b,c). In contrast to hM4R, hM4Di completely lost detectible basal activity and was similar to the negative control (Fig. 3c). This finding could also explain why most agonists of mAChRs are largely ACh-like compounds with a relatively small and extended scaffold to avoid affecting this hydrogen bonding network. Thus, once these small-scaffold agonists bind to the OBP, the connection would be further enhanced through the salt bridge interaction with D3x32 and π–cation interactions with the tyrosine lid (Figs. 2c and 3i).

In the DREADDs, although the TM3–TM6–TM7 network was broken by Y3x33C, it was re-established after binding of the DREADD actuator. First, the shorter side chain of cysteine eliminated the steric hindrance between TM3 and chemogenetic actuators, which led to antagonism of the WT receptors (as described above). This result was also supported by the mutagenesis data of $Y113^{3x33}A$, which could also be fully activated as $Y113^{3x33}C$ with about 15-fold less potency (Fig. 3b). Second, the basic amino group of actuators stabilized the hydrogen bond network among D3x32, Y7x38 and Y7x42 as the positively charged nitrogen of iperoxo. Third, the hydrogen bonds between the amino groups on the tricyclic ring and Y6x51 and N6x52, as well as the interactions between C3x33 and actuator, re-established the TM3–TM6 connection, which plays a similar part as the tyrosine lid does in WT mAChRs (Fig. 3j). The substituted cysteine not only formed a weak hydrogen bond with the amino group as Y6x51 but also had hydrophobic interactions with the tricyclic rings (Fig. 2a). To investigate the role of this cysteine residue, we generated two mutants, $Y113^{3x33}L$ and $Y113^{3x33}D$, and tested them using BRET assays. The results indicated that both mutations abolished the activity of the receptors in responding to ACh (Fig. 3a). In addition, the mutant $Y113^{3x33}L$ was activated more potently than $Y113^{3x33}A$ by DCZ, whereas the mutant Y113D displayed an even lower activity than the WT hM4R (Fig. 3b). Meanwhile, the surface expression level of Y113D was also significantly lower than the WT hM4R (Supplementary Fig. 4a), which suggested that the hydrophilic residue at position 3x33 not only affects receptor activation but also reduces receptor stability.

Last, although the mutation A5x461G alone could not enhance the DCZ-induced activation of hM4R, it substantially improved the potency of DCZ based on results with $Y113^{3x33}C$ (Fig. 3b). In our previous study[38], the same mutation (A5x461G) on the 5-hydroxytryptamine 2B receptor ($5\text{-}HT_{2B}R$) transformed the antagonist methysergide into a potent agonist by introducing more bulk tolerance in the binding pocket[38]. Similarly, in the hM3Dq–DCZ structure, the distance between the Cα of G5x461 and DCZ was appropriate and would induce a steric clash with the side chain of A5x461 of hM3R (Fig. 2a and Supplementary Fig. 6c). Consistent with this result, the docking poses of DCZ displayed displacements at hM3Dq (G5x461A) (Supplementary Fig. 6d), which might cause instability of DCZ in the binding pocket. This notion was further supported by the MD simulation of hM3Dq (G5x461A) with DCZ, which showed that the binding pose of DCZ largely rotated (Extended Data Fig. 6g,n,o and Supplementary Video 6).

Comparison of DREADD actuators

For chemogenetic actuators, it is important to maintain both high affinity and agonist activity for the DREADDs and diminish the affinity and eliminate any antagonist activity towards the WT receptor. In terms of their chemical structures, DCZ, CNO, C21, J52 and J60 are the analogues of CLZ. They share the same scaffold with a tricyclic core and a piperazine ring and contain all of the recognition elements described in the DREADD–DCZ recognition mode (Figs. 1a and 4a and Extended Data Fig. 7a). A comparison of CLZ and DCZ showed that DCZ had about 10-fold to 20-fold loss of binding affinities to the WT receptors compared with CLZ, but still activated the DREADDs at similar potencies as CLZ[13,17] (Fig. 5b,c). This result indicates that the 8-chloro group is important for the binding of CLZ to the WT receptors but not for the DREADDs. Thus, we docked CLZ, an antagonist to the WT hM3R, to the inactive-state structure of rM3R[30]. This experiment showed that its preferred binding pose is similar to TIO (Extended Data Fig. 7b,c). Specific interactions between the chloro group of CLZ and Y3x33 and Y6x51 of rM3R (Extended Data Fig. 7b), which are absent in the DREADD–DCZ recognition mode, might enhance the affinity of CLZ to the WT receptors. This result is consistent with the higher affinities of J52 and J60 to hM3R and hM4R than for DCZ[20]. Of the DREADD actuators, CNO is highly selective for DREADDs compared with other aminergic receptors, as its negatively charged *N*-oxide group interferes with the electrostatic interaction with D3x32, a highly conserved interaction for the aminergic receptors[39]. By contrast, compound 6 from our previous structure–activity relationship study[19] has a permanent positive charge, similar to CNO but without the negative charge, and is a potent full agonist for hM3Dq (Extended Data Fig. 7a). Thus, although the elimination of the positive charge of the compound provides enhanced selectivity, it also loses most of the affinity for the DREADDs.

PLP and OLP are two regulatory approved drugs that can activate DREADDs, and they could provide potential translational therapeutics for DREADD-treated central nervous system diseases. Of these, PLP was first discovered through high-throughput screening and validated as a potent agonist for hM3Dq[19]. Here we found that PLP is also a potent hM4Di agonist (Fig. 4c). The chemical structure of PLP is largely similar to DCZ, but without the 5-amino group on the tricyclic core. This difference causes PLP to lose important hydrogen bonding with N6x52 and results in much weaker agonist activities (Figs. 2a and 4a–c). Meanwhile, OLP was initially identified as a potent agonist for hM4Di through virtual similarity screening using C21 as a seed compound[16]. In our functional tests, OLP could also activate hM3Dq, albeit with lower potency than DCZ (Fig. 4b). Overall, OLP shares all of the important recognition elements we have identified in the DREADD–DCZ recognition mode (Figs. 2b and 4a). Notably, OLP is predicted to adopt an up-and-down flipped docking pose in our hM3Dq structure (Extended Data Fig. 7d). Although the hydrogen bond between the diazepine ring and Y6x51 was broken, a potential hydrogen bond was reformed with S3x36 through a rotamer change. Moreover, Y6x51 still formed an edge-to-face π-stacking interaction with the tricyclic core (Extended Data Fig. 7d). Taken together, although OLP might adopt a flipped binding pose, it is still predicted to form extensive interactions with surrounding residues to maintain affinities to DREADDs.

Finally, based on the similar chemical structure and docking pose of CLZ to TIO and QNB in the inactive-state structures, we wondered whether TIO and QNB could also activate DREADDs (Fig. 4a,d). This notion was supported by results from BRET assays and calcium flux assays for hM3Dq and cAMP Glo-sensor assays for hM4Di (Fig. 4e and Extended Data Fig. 5i–l). Both QNB and TIO displayed partial (BRET assay) or full agonist activities (cAMP Glo-sensor assay) for hM4Di but no agonist activities for hM3Dq (Fig. 4e and Extended Data Fig. 5j,l). These differential behaviours might be caused by the different activation energy barriers of hM3Dq and hM4Di, which we consider below. We also tested the compound AF-DX384 as a comparator, as it has a bulkier scaffold than QNB and TIO and shows a different binding mode by extending to the extracellular vestibule[40] (Fig. 2f and Extended Data Fig. 7a). In all the assays, AF-DX384 was inactive (Fig. 4e and Extended Data Fig. 5i–l).

Subtype of muscarinic receptor signalling

There are five members in the mAChR family, of which M1R, M3R and M5R couple to the $G_{q/11}$ family and M2R and M4R couple to the $G_{i/o}$ family. The overall structure and receptor–G protein interface of hM4Di–miniG_o are highly similar to that of hM2R–G_{oA}(ref. [26]) and hM4R–G_i(ref. [27]) (Supplementary Fig. 8). As the miniG_q-engaged hM3R and hM3Dq structures displayed high similarities with each other, we used the hM3Dq–miniG_q complex to investigate the features of M3R subtypes. A comparison between the G-protein-coupled hM3Dq and hM1R complexes indicated that the overall structures are similar, with RMSD values of 0.58 Å for the entire complex and 0.66 Å for the receptor alone (Fig. 5a and Extended Data Fig. 3b, c). Of note, in contrast to hM1R, the TM5 of hM3Dq does not form external helical turns (Fig. 5a). In the hM1R–G_{11} structure[26], L5x75 of the external helix forms extensive hydrophobic contacts with residues $F^{H5.06}$, $A^{H5.09}$ and $A^{H5.10}$ (superscript is common Gα numbering system[41]) of G_{11} (Extended Data Fig. 3f). However, in the hM3Dq–miniG_q structure, as miniG_q was developed on the basis of the G_s backbone[21], these

three residues are $R^{H5.06}$, $N^{H5.09}$ and $D^{H5.10}$, respectively (Extended Data Fig. 3f). Thus, this hydrophilic interface in miniG_q does not favour interactions with hydrophobic residues of TM5 of hM3Dq, which might affect the helical extension.

The analysis of the hM3Dq and miniG_q interface mainly focused on the interactions mediated by two featured residues, $N^{H5.24}$ and $E^{H5.22}$, of the $G_{q/11}$ subfamily (Fig. 5j). For the $N^{H5.24}$ residue (Gly in $G_{i/o}$, Glu in G_s and Met in $G_{12/13}$), it formed hydrogen bonds with R8x51 similar to in the hM1R–G_{11} structure (Fig. 5f,j). However, in the hM3Dq–miniG_q structure, $R177^{34x54}$ formed a salt bridge interaction with $E^{H5.22}$ and a hydrogen bond with $Y^{H5.23}$ (Fig. 5g). By contrast, in the hM1R–G_{11} structure, the side chain of $R135^{34x54}$ rotated downward and formed an electrostatic interaction with the main chain of $R^{hns1.02}$ at the αN-H1 joint loop of G_{11}. Moreover, the side chain of $R^{hns1.02}$ also formed an electrostatic interaction with the main chain of $R135^{34x54}$ (Fig. 5g). This pair of strong interactions might induce the upward displacement of the αN helix of G_{11} and a slight shift of intracellular loop 2 (ICL2) in hM1R compared with G_q and hM3Dq (Fig. 5a). Subsequently, G_{11} displayed mild rotation (Fig. 5a). Both types of interaction modes mediated by R34x54 have been observed in other $G_{q/11}$-engaged complexes. For example, in structures of miniG_q with the histamine H_1 receptor[42] and the orphan receptor MRGPRX4 (ref. [43]), R34x54 has a salt bridge interaction with $E^{H5.22}$ as in the hM3Dq–miniG_q structure. In addition, in structures of miniG_q with the cholecystokinin CCK_1 receptor[44] and the bradykinin B_1 receptor[45], R34x54 forms the salt bridge interaction with the joint loop as in the hM1R–G_{11} structure (Extended Data Fig. 8a–d). The mutagenesis data of these two arginine residues also showed that $R552^{8x51}$A substantially reduced the activation of both hM3R and hM3Dq. By contrast, $R177^{34x54}$A only had a moderate effect on receptor activation (Extended Data Fig. 5m,o), which indicates that the interaction pair R8x51–$N^{H5.24}$ is more crucial for G_q coupling of the hM3R subtype.

Notably, an extra electron-dense region was observed at the groove formed by TM3, TM4, TM5 and ICL2 in the hM3R–iperoxo structure, and a cholesteryl hemisuccinate (CHS) molecule was well modelled in the pocket (Fig. 5d,e). In the iperoxo-bound hM1R–G_{11} structure, there were also two CHS molecules in another two distinct pockets[26] (Extended Data Fig. 3g). These CHS molecules formed extensive hydrophobic contacts with surrounding residues. In a previous study[46], the P34x54R mutation in hM2R transformed it so that it can activate G_q signalling. However, the mutations R184A and R184M only slightly decreased the efficacies of hM3R (around 70% of the WT) and did not show significant effects on hM3Dq activation (Extended Data Fig. 5n,p). This result is consistent with the observation that the CHS molecule is only seen in the hM3R structure. In addition, sequence alignment showed that all three of these arginine residues (R34x54, R4x41 and R8x51) are conserved among the G_q-coupled subtypes (hM1R, hM3R and hM5R) (Fig. 5i). Taken together with the above structural and functional analyses, our findings suggest variable importance of the roles of these three arginines in subtype selectivity.

Although both DREADDs could be effectively activated by DCZ, the potency for hM3Dq is around 40-fold less than for hM4Di (Fig. 4b,c). However, as described above, the recognition modes of DCZ for hM3Dq and hM4Di were largely identical (Fig. 2a). To gain insights into the differences between hM3Dq and hM4Di, we compared the overall structures of these two DREADD complexes. Overall, the structure of hM3Dq–miniG_q was similar to hM4Di–miniG_o, with RMSD values of 1.05 Å for the entire complex and 0.72 Å for the receptor alone (Fig. 5b and Extended Data Fig. 3d,e). A notable difference was that the TM6 of hM4Di displayed a less outward displacement (about 1.9 Å, Cα of 6x33) in comparison with hM3Dq on the intracellular side (Fig. 5b and Extended Data Fig. 3e). Among the aminergic receptor families, only the mAChR and 5-HTR families have solved structures of both the $G_{q/11}$-engaged and $G_{i/o}$-engaged complexes. Notably, a comparison between 5-HT_{2A}R[22] and 5-HT_{1A}R[47] indicated a different feature from hM3Dq and hM4Di. Specifically, the outward displacement of TM6 in the 5-HT_{2A}R–miniG_q complex was less than in the 5-HT_{1A}R–G_i complex (Fig. 5c). Thus, with almost identical binding pockets of hM3Dq and hM4Di, a larger outward displacement of TM6 in hM3Dq suggests that there is a higher energy barrier during receptor activation. This speculation is supported by the functional data that all the DREADD actuators displayed lower potencies or efficacies for hM3Dq than hM4Di (Fig. 4b,c,e).

Two distinct G_q-coupling modes revealed

To determine the specificities for $G_q$coupling of the mAChRs, we compared the hM3Dq–miniG_q structure and with the 5-HT_{2A}R–miniG_q structure[22]. This comparison revealed two significant conformational differences of the α5 helices of G_q. One is a shift of the terminal residue $V^{H5.26}$ (Cα) of G_q to the side of the helix 8 (H8) about 6 Å and the other is the residue $N^{H5.24}$ featured in the $G_{q/11}$ family pointed to the opposite directions that are separated by the TM7–H8 loop (Fig. 5h). Unlike the interaction between $N^{H5.24}$ and R8x51 in the hM1R or hM3Dq complex, $N^{H5.24}$ formed a hydrogen bond with N8x47 in the 5-HT_{2A}R complex (Extended Data Fig. 9b). Accordingly, the cytoplasmic region of TM6 in 5-HT_{2A}R also displayed much less outward movement in comparison with hM3Dq or hM1R (Extended Data Fig. 9c). Thus, on the basis of these two distinct coupling conformations of the α5 helices of G_q, we named them the M1R mode and the 5-HT_{2A}R mode, respectively. To investigate the universality of this G_q-binding mode, we further analysed other structures of G_q-coupled complexes in the GPCRdb[48] (Extended Data Fig. 9d). Most of the complexes adopted the 5-HT_{2A}R mode, including the ghrelin receptor[49], bradykinin receptors (B_1 and B_2)[45], cholecystokinin receptors (CCK_1 and CCK_2)[50] and MRGPR receptors (MRGPRX2 and MRGPRX4)[43]. Only the histamine H_1 receptor[42] uses the M1R mode in both the α5 helix of G_q and the TM6 displacement (Extended Data Fig. 9c). In addition, $N^{H5.24}$ formed a hydrogen bond with $N474^{8x49}$ of the H_1 receptor, which resembled the $N^{H5.24}$–R^{8x51} hydrogen bond in the hM3Dq–miniG_q complex (Fig. 5f and Extended Data Fig. 8e).

Discussion

Chemogenetics has transformed neuroscience research by providing tools to remotely and reliably modulate neuronal activity and signalling[1–4]. Chemogenetic tools are used in nearly all areas of neuroscience and have catalysed insights into how discrete neuronal and non-neuronal elements within the nervous system affect behaviour, cognition, perception, sensation and most other processes encoded by neurons, glia and other cells within the brain. Chemogenetic tools are also widely used outside the nervous system to understand the roles of GPCR signalling in many organ systems, including the cardiovascular, metabolic, skeletal and immunological. The most widely used chemogenetic system is based on muscarinic receptors, and in this paper, we provided comprehensive structural insights into its ligand recognition, receptor activation and basal activity.

Even though DREADDs have been validated in vivo, with more than 17,000 papers citing the technology since 2007, the molecular mechanisms by which DREADDs recognize new chemogenetic actuators have remained unknown. Here we provided detailed molecular insights into the mechanisms responsible for the distinct pharmacology of muscarinic-based DREADDs and also provided dynamics-based insights into the low level of basal (for example, constitutive) activity that is key to the utility of DREADD use in vivo. Collectively, these findings clarify how these receptors, which were generated by directed evolution, achieve their selectivity and efficacy. Going forwards, these findings will accelerate the structure-guided discovery of new chemogenetic actuators that promise to further transform both basic and translational neuroscience.

Online content

Any methods, additional references, Nature Portfolio reporting summaries, source data, extended data, supplementary information, acknowledgements, peer review information; details of author contributions and competing interests; and statements of data and code availability are available at https://doi.org/10.1038/s41586-022-05489-0.

1. Urban, D. J. & Roth, B. L. DREADDs (designer receptors exclusively activated by designer drugs): chemogenetic tools with therapeutic utility. *Annu. Rev. Pharmacol. Toxicol.* **55**, 399–417 (2015).
2. Roth, B. L. DREADDs for neuroscientists. *Neuron* **89**, 683–694 (2016).
3. Roth, B. L. How structure informs and transforms chemogenetics. *Curr. Opin. Struct. Biol.* **57**, 9–16 (2019).
4. Wang, L. et al. Use of DREADD technology to identify novel targets for antidiabetic drugs. *Annu. Rev. Pharmacol. Toxicol.* **61**, 421–440 (2021).
5. Armbruster, B. N., Li, X., Pausch, M. H., Herlitze, S. & Roth, B. L. Evolving the lock to fit the key to create a family of G protein-coupled receptors potently activated by an inert ligand. *Proc. Natl Acad. Sci. USA* **104**, 5163–5168 (2007).
6. Boyden, E. S., Zhang, F., Bamberg, E., Nagel, G. & Deisseroth, K. Millisecond-timescale, genetically targeted optical control of neural activity. *Nat. Neurosci.* **8**, 1263–1268 (2005).
7. Isberg, V. et al. Generic GPCR residue numbers—aligning topology maps while minding the gaps. *Trends Pharmacol. Sci.* **36**, 22–31 (2015).
8. Hu, J. et al. A G protein-biased designer G protein-coupled receptor useful for studying the physiological relevance of $G_{q/11}$-dependent signaling pathways. *J. Biol. Chem.* **291**, 7809–7820 (2016).
9. Nakajima, K. & Wess, J. Design and functional characterization of a novel, arrestin-biased designer G protein-coupled receptor. *Mol. Pharmacol.* **82**, 575–582 (2012).
10. Guettier, J. M. et al. A chemical-genetic approach to study G protein regulation of β cell function in vivo. *Proc. Natl Acad. Sci. USA* **106**, 19197–19202 (2009).
11. Inoue, A. et al. Illuminating G-protein-coupling selectivity of GPCRs. *Cell* **177**, 1933–1947. e25 (2019).
12. Bender, D., Holschbach, M. & Stöcklin, G. Synthesis of n.c.a. carbon-11 labelled clozapine and its major metabolite clozapine-*N*-oxide and comparison of their biodistribution in mice. *Nucl. Med. Biol.* **21**, 921–925 (1994).
13. Gomez, J. L. et al. Chemogenetics revealed: DREADD occupancy and activation via converted clozapine. *Science* **357**, 503–507 (2017).
14. Jann, M. W., Lam, Y. W. & Chang, W. H. Rapid formation of clozapine in guinea-pigs and man following clozapine-*N*-oxide administration. *Arch. Int. Pharmacodyn. Ther.* **328**, 243–250 (1994).
15. Roth, B. L., Sheffler, D. J. & Kroeze, W. K. Magic shotguns versus magic bullets: selectively non-selective drugs for mood disorders and schizophrenia. *Nat. Rev. Drug Discov.* **3**, 353–359 (2004).
16. Weston, M. et al. Olanzapine: a potent agonist at the hM4D(Gi) DREADD amenable to clinical translation of chemogenetics. *Sci. Adv.* **5**, eaaw1567 (2019).
17. Nagai, Y. et al. Deschloroclozapine, a potent and selective chemogenetic actuator enables rapid neuronal and behavioral modulations in mice and monkeys. *Nat. Neurosci.* **23**, 1157–1167 (2020).
18. Thompson, K. J. et al. DREADD agonist 21 is an effective agonist for muscarinic-based DREADDs in vitro and in vivo. *ACS Pharmacol. Transl. Sci.* **1**, 61–72 (2018).
19. Chen, X. et al. The first structure–activity relationship studies for designer receptors exclusively activated by designer drugs. *ACS Chem. Neurosci.* **6**, 476–484 (2015).
20. Bonaventura, J. et al. High-potency ligands for DREADD imaging and activation in rodents and monkeys. *Nat. Commun.* **10**, 4627 (2019).
21. Nehme, R. et al. Mini-G proteins: novel tools for studying GPCRs in their active conformation. *PLoS ONE* **12**, e0175642 (2017).
22. Kim, K. et al. Structure of a hallucinogen-activated G_q-coupled 5-HT_{2A} serotonin receptor. *Cell* **182**, 1574–1588.e19 (2020).
23. Garcia-Nafria, J., Nehme, R., Edwards, P. C. & Tate, C. G. Cryo-EM structure of the serotonin 5-HT_{1B} receptor coupled to heterotrimeric G_o. *Nature* **558**, 620–623 (2018).
24. Zhang, S. et al. Inactive and active state structures template selective tools for the human 5-HT_{5A} receptor. *Nat. Struct. Mol. Biol.* **29**, 677–687 (2022).
25. Duan, J. et al. Cryo-EM structure of an activated VIP1 receptor–G protein complex revealed by a NanoBiT tethering strategy. *Nat. Commun.* **11**, 4121 (2020).
26. Maeda, S., Qu, Q., Robertson, M. J., Skiniotis, G. & Kobilka, B. K. Structures of the M1 and M2 muscarinic acetylcholine receptor/G-protein complexes. *Science* **364**, 552–557 (2019).
27. Wang, J. et al. The unconventional activation of the muscarinic acetylcholine receptor M4R by diverse ligands. *Nat. Commun.* **13**, 2855 (2022).
28. Liu, H. et al. Structure-guided development of selective M3 muscarinic acetylcholine receptor antagonists. *Proc. Natl Acad. Sci. USA* **115**, 12046–12050 (2018).
29. Thorsen, T. S., Matt, R., Weis, W. I. & Kobilka, B. K. Modified T4 lysozyme fusion proteins facilitate G protein-coupled receptor crystallogenesis. *Structure* **22**, 1657–1664 (2014).
30. Kruse, A. C. et al. Structure and dynamics of the M3 muscarinic acetylcholine receptor. *Nature* **482**, 552–556 (2012).
31. Kenakin, T., Watson, C., Muniz-Medina, V., Christopoulos, A. & Novick, S. A simple method for quantifying functional selectivity and agonist bias. *ACS Chem. Neurosci.* **3**, 193–203 (2012).
32. Wess, J., Maggio, R., Palmer, J. R. & Vogel, Z. Role of conserved threonine and tyrosine residues in acetylcholine binding and muscarinic receptor activation. A study with M3 muscarinic receptor point mutants. *J. Biol. Chem.* **267**, 19313–19319 (1992).
33. Heitz, F. et al. Site-directed mutagenesis of the putative human muscarinic M2 receptor binding site. *Eur. J. Pharmacol.* **380**, 183–195 (1999).
34. Nawaratne, V. et al. New insights into the function of M4 muscarinic acetylcholine receptors gained using a novel allosteric modulator and a DREADD (designer receptor exclusively activated by a designer drug). *Mol. Pharmacol.* **74**, 1119–1131 (2008).
35. Abdul-Ridha, A., Lane, J. R., Sexton, P. M., Canals, M. & Christopoulos, A. Allosteric modulation of a chemogenetically modified G protein-coupled receptor. *Mol. Pharmacol.* **83**, 521–530 (2013).
36. Haga, K. et al. Structure of the human M2 muscarinic acetylcholine receptor bound to an antagonist. *Nature* **482**, 547–551 (2012).
37. Jumper, J. et al. Highly accurate protein structure prediction with AlphaFold. *Nature* **596**, 583–589 (2021).
38. McCorvy, J. D. et al. Structural determinants of 5-HT_{2B} receptor activation and biased agonism. *Nat. Struct. Mol. Biol.* **25**, 787–796 (2018).
39. Wacker, D., Stevens, R. C. & Roth, B. L. How ligands illuminate GPCR molecular pharmacology. *Cell* **170**, 414–427 (2017).
40. Suno, R. et al. Structural insights into the subtype-selective antagonist binding to the M2 muscarinic receptor. *Nat. Chem. Biol.* **14**, 1150–1158 (2018).
41. Flock, T. et al. Universal allosteric mechanism for Gα activation by GPCRs. *Nature* **524**, 173–179 (2015).
42. Xia, R. et al. Cryo-EM structure of the human histamine H_1 receptor/G_q complex. *Nat. Commun.* **12**, 2086 (2021).
43. Cao, C. et al. Structure, function and pharmacology of human itch GPCRs. *Nature* **600**, 170–175 (2021).
44. Mobbs, J. I. et al. Structures of the human cholecystokinin 1 (CCK1) receptor bound to G_s and G_q mimetic proteins provide insight into mechanisms of G protein selectivity. *PLoS Biol.* **19**, e3001295 (2021).
45. Yin, Y. L. et al. Molecular basis for kinin selectivity and activation of the human bradykinin receptors. *Nat. Struct. Mol. Biol.* **28**, 755–761 (2021).
46. Blin, N., Yun, J. & Wess, J. Mapping of single amino acid residues required for selective activation of $G_{q/11}$ by the m3 muscarinic acetylcholine receptor. *J. Biol. Chem.* **270**, 17741–17748 (1995).
47. Xu, P. et al. Structural insights into the lipid and ligand regulation of serotonin receptors. *Nature* **592**, 469–473 (2021).
48. Kooistra, A. J. et al. GPCRdb in 2021: integrating GPCR sequence, structure and function. *Nucleic Acids Res.* **49**, D335–D343 (2021).
49. Wang, Y. et al. Molecular recognition of an acyl-peptide hormone and activation of ghrelin receptor. *Nat. Commun.* **12**, 5064 (2021).
50. Zhang, X. et al. Structures of the human cholecystokinin receptors bound to agonists and antagonists. *Nat. Chem. Biol.* **17**, 1230–1237 (2021).

Publisher's note Springer Nature remains neutral with regard to jurisdictional claims in published maps and institutional affiliations.

Springer Nature or its licensor (e.g. a society or other partner) holds exclusive rights to this article under a publishing agreement with the author(s) or other rightsholder(s); author self-archiving of the accepted manuscript version of this article is solely governed by the terms of such publishing agreement and applicable law.

© The Author(s), under exclusive licence to Springer Nature Limited 2022

Methods

Construction and expression of the receptor–G protein complex

For the cryogenic electron microscopy (cyro-EM) studies, based on the genes that encode hM3R (UniProt identifier: P20309) and hM4R (UniProt identifier: P08173), the human M3Dq and M4Di constructs were generated by introducing two site-specific mutations (Y3x33C and A5x361G) and cloned into a modified pFastBac1 vector (Invitrogen) containing a haemagglutinin signal peptide followed by Flag-tag, His_{10}-tag and a TEV protease site at the N terminus. For the miniG_q and miniG_o heterotrimeric complexes, we used the same constructs as used to construct the 5-HT_{2A}R–miniGq (ref. [22]) and 5-HT_{5A}R–miniG_o (ref. [24]) complexes. For the hM3Dq–miniG_q–CNO and hM3R–miniG_q–iperoxo complexes, the LgBit and HiBit segments were fused to the carboxy terminus of the hM3Dq or hM3R receptor and the Gβ subunit after a 15-G_S linker, respectively, to enhance the stability of the full complex[25]. Schematic diagrams of the constructs are provided in Extended Data Fig. 1a–c.

The Bac-to-Bac baculovirus expression system (Invitrogen) was used to generate the recombinant baculovirus for protein expression. Baculoviruses of hM3Dq, hM4Di, hM3R–LgBit or hM3Dq–LgBit, corresponding miniG_o–$G\beta_1\gamma_2$ or miniG_q–$G\beta_1\gamma_2$ (without or with HiBit), and scFv16 were co-expressed by infecting Sf9 cells at a density of 2.8×10^6 cells per ml at multiplicity of infection ratio of 3:1:1, respectively. Cells were collected by centrifugation 48 h after infection and stored at −80 °C for future use.

Receptor–G protein complex purification

The cell pellet of the hM3Dq–miniG_q–scFv16 complex was thawed on ice and incubated with a buffer containing 20 mM HEPES pH 7.5, 50 mM NaCl, 1 mM $MgCl_2$, proteinase inhibitor and 5 μM DCZ at room temperature. After 1.5 h, the cell suspension was homogenized. The membrane was collected by centrifugation at 70,000*g* for 30 min and solubilized using 40 mM HEPES pH 7.5, 100 mM NaCl, 5% (w/v) glycerol, 0.5% (w/v) lauryl maltose neopentyl glycol (LMNG; Anatrace, NG310) and 0.05% (w/v) CHS for 5 h at 4 °C. The solubilized proteins in the supernatants were isolated by ultracentrifugation at 160,000*g* for 30 min and then incubated overnight at 4 °C with TALON IMAC resin and 20 mM imidazole. The resin was collected the next day and washed with 25 column volumes of 20 mM HEPES pH 7.5, 100 mM NaCl, 30 mM imidazole, 0.01% (w/v) LMNG, 0.001% (w/v) CHS and 1 μM DCZ. The protein was then eluted using the same buffer supplemented with 250 mM imidazole. Eluted protein was concentrated and subjected to size-exclusion chromatography on a Superdex 200 Increase 10/300 column (GE Healthcare) that was pre-equilibrated with 20 mM HEPES pH 7.5, 100 mM NaCl, 1 μM DCZ, 0.00075% (w/v) LMNG, 0.00025 (w/v) glyco-diosgenin (Anatrace, GDN101) and 0.00075% (w/v) CHS. Peak fractions were collected and incubated with 15 μl of His-tagged PreScission protease (GenScript, Z03092-500) and 2 μl PNGase F (NEB, P0708S) at 4 °C overnight to remove the N-terminal BRIL and potential glycosylation products. The protein was concentrated and further purified the next day by size-exclusion chromatography using the same buffer. Peak fractions were collected and concentrated to around 5 mg ml^{-1}. The CNO-bound hM3Dq–miniG_q–scFv16, iperoxo-bound hM3R–miniG_q–scFv16 and DCZ-bound hM4Di–miniG_o–scFv16 complexes were purified using the same protocol.

Cryo-EM data collection, 3D reconstitution, model building and refinement

The cryo-EM data collection and processing of the DREADD or WT complexes followed a previously published protocol[51]. The samples (3.2 μl) were applied to glow-discharged Quantifoil R1.2/1.3 Au300 holey carbon grids (Ted Pella) individually and were flash-frozen in a liquid ethane–propane (40:60) mixture using a Vitrobot Mark IV (FEI) set at 4 °C and 100% humidity with a blot time range from 2.5 to 5 s. Images were collected using a 200 keV Talos Artica with a Gatan K3 direct electron detector at a physical pixel size of 0.88 Å. Micrograph-recorded movies were automatically collected using SerialEM using a multishot array[52]. Data were collected at an exposure dose rate of around 15 electrons per pixel per s as recorded from counting mode. Images were recorded for about 1.7–2.7 s in 60 subframes to give a total exposure dose of approximately 29–48 electrons per $Å^2$. Following manual inspection and curation of the micrographs, particles from each dataset were selected using the Blob particle picker, and initial 2D classification produced templates for subsequent template picking. After one round of 2D classification and selection in cryoSPARC, a subset of the selected particles was used as a training set for Topaz, and the particles were re-picked from the micrographs using Topaz[53] and subjected to 2D classification and 3D classification. The select classified picked particle coordinates from the three sets were next merged to produce a subset of distinct particles that survived 2D classification (that is, duplicates were removed with a radius of 75 pixels). All subsequent 3D classification and refinement steps were performed within cryoSPARC[54,55]. Multiple rounds of multi-reference refinement resolved the final stack of particles that produced a map with a resolution reported in Extended Data Table 1 (by FSC using the 0.143 Å cut-off criterion)[56] after Global CTF refinement and post-processing including soft masking, B-factor sharpening in cryoSPARC and filtering by local resolution[57] to generate the post-processed sharpened map. Alternative post-sharpening was performed on the two half-maps using deepEMhancer[58]. For more details, see Extended Data Table 1 and Extended Data Fig. 2.

Maps from deepEMhancer were used for map building, refinement and subsequent structural interpretation. The hM1R–G_{11} (Protein Data Bank (PDB) identifier: 6OIJ) and hM2R–G_{oA} (PDB identifier: 6OIK) structures were used as the initial model for the hM3Dq–miniG_q and hM4Di–miniG_o complexes and docked into the cryo-EM map using Chimera[59] followed by iterative manual adjustment in COOT[60] and Phenix.real_space_refine in Phenix[61]. The model statistics were validated using Molprobity[62]. Structural figures were prepared using Chimera or Pymol (https://pymol.org/2/).

BRET assay

Agonist-stimulated G protein activation of WT and mutant hM3Dq, hM4Di, hM3R or hM4R were performed using TruPath BRET2 assays and transient transfection[63]. For the G_q activation assay of hM3Dq or hM3R, HEK293T cells (American Type Culture Collection (ATCC), CRL-11268; 59587035; mycoplasma free) were co-transfected using Transit (Mirus Bio) in a 2:1:1:2 ratio of hM3R or hM3Dq, G_q-Rluc, $G\beta_3$ and GFP2-γ9, respectively. For the G_oA activation assay of hM4Di or hM4R, HEK293T cells were co-transfected in the same ratio 2:1:1:2 of hM4R or hM4Di, G_oA-Rluc, $G\beta_1$ and GFP2-γ2, respectively. After at least 24 h, transfected cells were plated in poly-L-lysine-coated 96-well white clear-bottom cell culture plates in plating medium (DMEM containing 1% (v/v) dialysed FBS, 1 IU ml^{-1} penicillin G and 100 μg ml^{-1} streptomycin) at a density of 40,000 cells in 200 μl per well and incubated overnight. The following day, the medium was aspirated and cells were washed once with 60 μl of drug buffer (1×HBSS, 20 mM HEPES, pH 7.4). Then 60 μl of *Renilla* luciferase (Rluc) substrate coelenterazine 400a (Nanolight, 5 μM final concentration) solution was added per well, and drug stimulation was performed with the addition of 30 μl of 3× drug dilution in drug dilution buffer (1×HBSS, 20 mM HEPES, 0.3% (w/v) BSA, pH 7.4) per well and incubated at room temperature. After 10 min of incubation, plates were read for luminescence at 400 nm and fluorescent GFP2 emission at 515 nm for 1 s per well using Pherastar. The ratio of GFP2/Rluc was calculated per well and plotted as a function of drug concentration using GraphPad Prism 9.2.

FLIPR Ca^{2+} assay

Tetracycline-inducible hM3R and hM3Dq stable cells (Flp-In T-REx-293 cells, derived from HEK293 cells (ATCC, CRL-1573; mycoplasma

free)) were maintained in DMEM containing 10% (v/v) FBS, 100 units per ml penicillin G, 100 µg ml^{-1} streptomycin, 100 µg ml^{-1} hygromycin B and 15 µg ml^{-1} blasticidin. On the day of the assay, cells were plated into poly-L-lysine-coated 384-well black clear-bottom cell culture plates with DMEM, supplemented with 1% (v/v) dialysed FBS, at a density of 15,000 cells in 40 µl per well overnight. The medium was removed and cells were incubated with 20 µl of calcium dye (FLIPR Calcium 4 Assay kit, Molecular Devices) diluted in assay buffer (1×HBSS, 2.5 mM probenecid, 20 mM HEPES, pH 7.4) for 1 h at 37 °C and 20 min at room temperature in the dark. To measure the agonist activity of receptors, drug plates were prepared with increasing concentrations of test compound at 3 times the desired final concentration using drug buffer (1×HBSS, 20 mM HEPES, 0.1% (w/v) BSA, pH 7.4). Once loaded in FLIPR^{TETRA} (Molecular Devices), basal fluorescence was measured for 10 s, then 10 µl of test compounds was added followed by continued fluorescence measurement for an additional 180 s. Peak fluorescence intensity within 60 s after drug addition was exported. Data were analysed using 'log(agonist) versus response' in GraphPad Prism 9.2.

Split-luciferase based cAMP reporter assays

HEK293T (ATCC, CRL-11268; 59587035; mycoplasma free) cells co-transfected hM4R or hM4Di along with a split-luciferase-based cAMP biosensor (Glo-Sensor 22F, Promega) were seeded in poly-L-lysine-coated 384-well white clear bottom cell culture plates (Greiner; 15,000 cells per well, 40 µl per well) in DMEM containing 1% (v/v) dialysed FBS. The next day, the culture medium was removed and 20 µl per well of drug buffer was added followed by the addition of 10 µl of 3× drug solutions for 15 min at room temperature. To measure agonist activity for $G_{i/o}$-coupled receptors, 10 µl luciferin (44 mM final concentration) supplemented with isoproterenol (200 nM final concentration was added to activate G_s signalling through endogenous β_2-adrenergic receptors) and luminescence intensity was quantified 15 min later. Data were analysed using 'log(agonist) versus response' in GraphPad Prism 9.2.

To measure the basal activities of hM4R and hM4Di, after 12 h of the transient co-transfection of the HEK293T (ATCC, CRL-11268; 59587035; mycoplasma free) cells by hM4R, hM4Di, pCNDA3 or only with a cAMP Glo-Sensor biosensor, cells were suspended in DMEM supplemented with 1% dialysed FBS and then plated in poly-L-lysine-coated 384-well plates (Greiner). After 6 h, buffer or 100 ng ml^{-1} pertussis toxin was added to the cells for another 12 h. The culture medium was removed and then 20 µl luciferin (44 mM final concentration) supplemented with 200 nM isoproterenol was added to the wells. After 15 min incubation, the plate was read in the luminescence mode of PHERAstar. The data were calculated by the fold of pertussis-toxin-treated over buffer-treated luminescence intensity, and figures were generated using GraphPad Prism 9.2.

MD simulation

Receptors alone (hM3R or hM3Dq) were created by removing the G-protein heterotrimers and other accessory proteins. Each receptor was then prepared using Maestro v.12.9 (Schrodinger). The receptors were then aligned to the PDB: 4DAJ structure from the Orientations of Proteins in Membranes database[64]. These resulting structures were then placed in a bilayer using the membrane bilayer builder in CHARMM-GUI[65–68]. In brief, the receptors were inserted into a membrane of palmitoyloleoyl-phosphatidylcholine and sodium and chloride ions were added to neutralize each system at a concentration of 150 mM. Parameterization of each ligand was done using the CHARMM-GUI process during system construction. Each structure was simulated using randomly assigned initial velocities for 3 independent runs and at least 0.8–1.5 µs for a total of 2.4–4.5 µs. The CHARMM36m force field was used for all runs as well as the TIP3P model for waters[69,70]. Simulations were run using AMBER20.12 (ref. [71]) and the Compute Unified Device Architecture version of Particle-Mesh Ewald Molecular Dynamics on a single GPU. Energy minimization was carried out, and the suggested protocol from the CHARMM-GUI output was used to equilibrate the system. The production simulations were performed using the NPT ensemble at 310 K and 1 bar using a Langevin thermostat and Monte Carlo barostat. A time step of 2.0 fs was used and nonbonded interactions were cut-off at 9.0 Å and electrostatic interactions were calculated using the particle-mesh Ewald method. To constrain the length of bonds to hydrogen atoms, SHAKE was used, and snapshots of the simulations were saved every 100 ps.

Trajectories were re-imaged and aligned using the python package pytraj, which is bound to the cpptraj program[72]. Distances were also calculated using pytraj. Snapshots of the trajectories were visualized and output using Visual Molecular Dynamics[73], PyMOL (https://pymol.org/2/) or ChimeraX[74]. All the plots were generated using the python-based plotting packages Matplotlib or Seaborn.

Molecular docking

All the models used for docking (active-state hM3R (this work), hM3Dq (this work) and inactive-state rM3R (PDB: 4DAJ)) were prepared using the Protein Preparation Wizard in Maestro v.12.9 (Schrodinger) to fill in the missing side chains, optimize hydrogen bond assignments and perform a restrained minimization. The ligands were prepared by LigPrep using the OPLS4 forcefield and the protonation state was determined using Epik at pH 7.0. At most, 32 different conformers were generated for each compound. Receptor grid generation was done using the placement of the ligands with the solved structures, and compounds were ultimately docked using the standard precision method of Glide. The docking protocol was validated by redocking the compound that was in the experimental structure (that is, iperoxo was redocked into hM3R–iperoxo).

Radioligand binding assays

Binding assays were set up in 96-well plates in standard binding buffer (50 mM Tris, 0.1 mM EDTA, 10 mM $MgCl_2$, 0.1% (m/v) BSA and 0.01% (m/v) ascorbic acid, pH 7.4). For the competition binding assay, 50 µl each of ^{3}H-QNB, drug solution (3×) and homogeneous hM3R, hM4R, hM3Dq or hM4Di membrane solution were incubated in a 96-well plate. Reactions were incubated for 2 h at room temperature in the dark and terminated by rapid vacuum filtration onto chilled 0.3% PEI-soaked GF/A filters followed by three quick washes with cold washing buffer (50 mM Tris-HCl, pH 7.4) and read. Results were analysed using the equation 'one-site fit Ki' in GraphPad Prism 9.2.

Cell surface expression of receptors

Cell-surface expressions of WT and mutant hM3R, hM3Dq, hM4R and hM4Di were measured using ELISA chemiluminescence as previously described[24]. In brief, 48 h after transfection, cells plated in 384 white-well plates were fixed with 20 µl 4% (v/v) paraformaldehyde per well for 10 min at room temperature. The cells were washed with 40 µl PBS per well twice and then incubated with 20 µl per well 5% (m/V) BSA in PBS for 1 h. Then the cells were incubated with an anti-Flag–horseradish peroxidase-conjugated antibody (Sigma-Aldrich, A8592) diluted 1:10,000 in 5% (m/V) BSA in PBS for 1 h at room temperature. After washing 5 times with 80 µl PBS per well, 20 µl super signal ELISA pico substrate (Thermo Fisher, 37070) was added to the well for development of the signal, and the luminescence was counted using PHERAstar FSX (BMG Labtech). The luminescence signal was analysed using GraphPad Prism 9.2 and data were normalized to the signal of WT or DREADD receptors.

Reporting summary

Further information on research design is available in the Nature Portfolio Reporting Summary linked to this article.

Data availability

The structures of the hM3Dq–miniG_q–DCZ, hM4Di–miniG_o–DCZ, hM3Dq–miniG_q–CNO, hM3R–miniG_q–iperoxo and hM3R–iperoxo (local refinement) complexes have been deposited into the PDB (EMDB) databases under accession codes 8E9W (EMD-27966), 8E9X (EMD-27967), 8E9Y (EMD-27968), 8E9Z (EMD-27969) and 8EA0 (EMD-27970), respectively. The cryo-EM micrographs of hM3D$_q$–miniG_q–DCZ, hM4Di–miniG_o–DCZ, hM3Dq–miniG_q–CNO and hM3R–miniG_q–iperoxo have been deposited in the EMPIAR database (https://www.ebi.ac.uk/empiar/) with accession numbers EMPIAR-11185, EMPIAR-11184, EMPIAR-11193 and EMPIAR-11194, respectively. Source data are provided with this paper.

51. Peck, J. V., Fay, J. F. & Strauss, J. D. High-speed high-resolution data collection on a 200 keV cryo-TEM. *IUCrJ* **9**, 243–252 (2022).
52. Mastronarde, D. N. Automated electron microscope tomography using robust prediction of specimen movements. *J. Struct. Biol.* **152**, 36–51 (2005).
53. Bepler, T., Kelley, K., Noble, A. J. & Berger, B. Topaz-Denoise: general deep denoising models for cryoEM and cryoET. *Nat. Commun.* **11**, 5208 (2020).
54. Punjani, A., Rubinstein, J. L., Fleet, D. J. & Brubaker, M. A. cryoSPARC: algorithms for rapid unsupervised cryo-EM structure determination. *Nat. Methods* **14**, 290–296 (2017).
55. Punjani, A., Zhang, H. & Fleet, D. J. Non-uniform refinement: adaptive regularization improves single-particle cryo-EM reconstruction. *Nat. Methods* **17**, 1214–1221 (2020).
56. Rosenthal, P. B. & Henderson, R. Optimal determination of particle orientation, absolute hand, and contrast loss in single-particle electron cryomicroscopy. *J. Mol. Biol.* **333**, 721–745 (2003).
57. Heymann, J. B. & Belnap, D. M. Bsoft: image processing and molecular modeling for electron microscopy. *J. Struct. Biol.* **157**, 3–18 (2007).
58. Sanchez-Garcia, R. et al. DeepEMhancer: a deep learning solution for cryo-EM volume post-processing. *Commun. Biol.* **4**, 874 (2021).
59. Pettersen, E. F. et al. UCSF Chimera—a visualization system for exploratory research and analysis. *J. Comput. Chem.* **25**, 1605–1612 (2004).
60. Emsley, P. & Cowtan, K. Coot: model-building tools for molecular graphics. *Acta Crystallogr. D* **60**, 2126–2132 (2004).
61. Adams, P. D. et al. PHENIX: a comprehensive Python-based system for macromolecular structure solution. *Acta Crystallogr. D* **66**, 213–221 (2010).
62. Chen, V. B. et al. MolProbity: all-atom structure validation for macromolecular crystallography. *Acta Crystallogr. D* **66**, 12–21 (2010).
63. Olsen, R. H. J. et al. TRUPATH, an open-source biosensor platform for interrogating the GPCR transducerome. *Nat. Chem. Biol.* **16**, 841–849 (2020).
64. Lomize, M. A., Pogozheva, I. D., Joo, H., Mosberg, H. I. & Lomize, A. L. OPM database and PPM web server: resources for positioning of proteins in membranes. *Nucleic Acids Res.* **40**, D370–D376 (2012).
65. Brooks, B. R. et al. CHARMM: the biomolecular simulation program. *J. Comput. Chem.* **30**, 1545–1614 (2009).
66. Jo, S., Kim, T., Iyer, V. G. & Im, W. CHARMM-GUI: a web-based graphical user interface for CHARMM. *J. Comput. Chem.* **29**, 1859–1865 (2008).
67. Lee, J. et al. CHARMM-GUI input generator for NAMD, GROMACS, AMBER, OpenMM, and CHARMM/OpenMM simulations using the CHARMM36 additive force field. *J. Chem. Theory Comput.* **12**, 405–413 (2016).
68. Wu, E. L. et al. CHARMM-GUI membrane builder toward realistic biological membrane simulations. *J. Comput. Chem.* **35**, 1997–2004 (2014).
69. Huang, J. et al. CHARMM36m: an improved force field for folded and intrinsically disordered proteins. *Nat. Methods* **14**, 71–73 (2017).
70. Klauda, J. B. et al. Update of the CHARMM all-atom additive force field for lipids: validation on six lipid types. *J. Phys. Chem. B* **114**, 7830–7843 (2010).
71. Case, D. A. et al. AMBER v.2020 (Univ. of California, San Francisco, 2020).
72. Roe, D. R. & Cheatham, T. E. PTRAJ and CPPTRAJ: software for processing and analysis of molecular dynamics trajectory data. *J. Chem. Theory Comput.* **9**, 3084–3095 (2013).
73. Humphrey, W., Dalke, A. & Schulten, K. VMD: visual molecular dynamics. *J. Mol. Graphics* **14**, 33–38 (1996).
74. Pettersen, E. F. et al. UCSF ChimeraX: structure visualization for researchers, educators, and developers. *Protein Sci.* **30**, 70–82 (2021).

Acknowledgements This work was supported by NIH grant U24DK116194, the NIMH Psychoactive Drug Screening Program and the Michael Hooker Distinguished Professorship to B.L.R. We thank J. Peck and J. Strauss of the UNC CryoEM Core Facility for their technical assistance in this project. The Titan X Pascal used for this research was donated to J.F.F. by the NVIDIA Corporation.

Author contributions S.Z. designed the experiments, performed the cloning, expression and purification of transducer-coupled DREADD or WT complexes, built and refined the models, performed mutagenesis and functional studies, performed the binding and ELISA assays, and prepared the figures, tables and manuscript. R.H.G. performed and analysed the docking and MD simulations. X.-P.H. performed cAMP Glo-Sensor and calcium flux experiments. Y.L. assisted in the functional experiments. B.E.K. and C.C. assisted in the protein expression experiments. J.F.F. made the grids and collected and processed the cryo-EM data. B.L.R supervised the entire project and prepared the manuscript.

Competing interests The authors declare no competing interests.

Additional information
Supplementary information The online version contains supplementary material available at https://doi.org/10.1038/s41586-022-05489-0.

Correspondence and requests for materials should be addressed to Jonathan F. Fay or Bryan L. Roth.

Peer review information *Nature* thanks Beili Wu and the other, anonymous, reviewer(s) for their contribution to the peer review of this work. Peer reviewer reports are available.

Reprints and permissions information is available at http://www.nature.com/reprints.

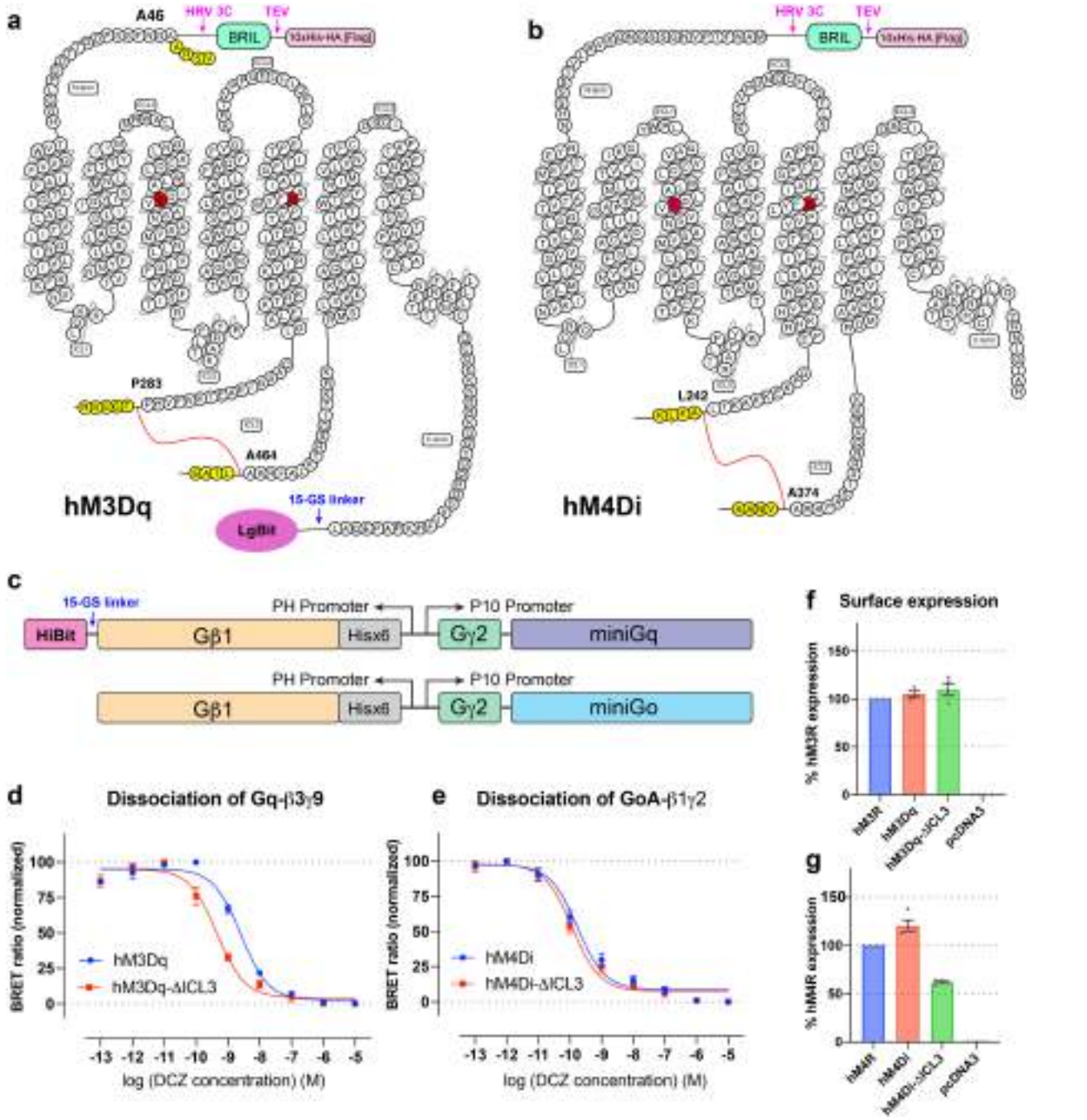

Extended Data Fig. 1 | Schematic diagrams of the constructs used in this study. a-b, Modified snake diagrams of hM3Dq and hM4Di from the GPCRdb including the N-terminal and ICL3 truncation sites. The LgBit was fused at the C terminus of the hM3Dq receptor. DREADD mutation sites are indicated by red circles. Residues in yellow circles were removed from the expression constructs. **c**, Schematic diagram of the 3-in-1 vector (pFastDual plasmid-based) for the expression of miniGq or miniGo. The HiBit was fused at the C-terminus of the Gβ subunit. **d-e**, The activities of intact and ICL3 deletions of hM3Dq (**d**) or hM4Di (**e**) under the stimulation by DCZ, respectively. See Supplementary Table 4 for fitted parameter values that represent the mean ± SEM of n = 4 biologically independent experiments. **f-g**, Surface expression levels of intact and ICL3 deletions of hM3Dq and hM4Di. The WT hM3R and hM4R are also included as controls. Data represent the mean ± SEM of n = 3 biologically independent experiments. See Supplementary Table 11 for the details.

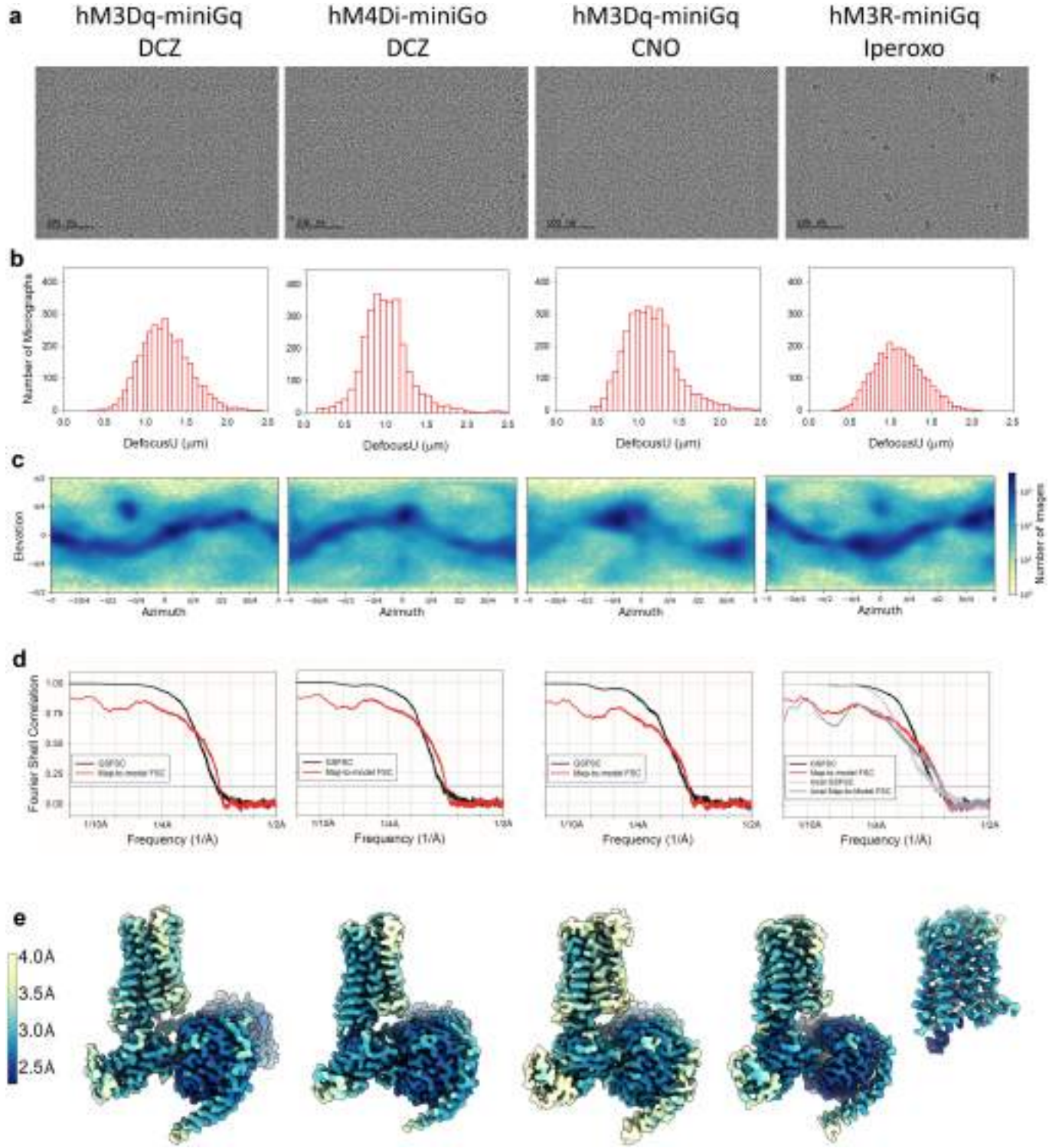

Extended Data Fig. 2 | CryoEM analysis for the complexes of DCZ-bound hM3Dq-miniGq, DCZ-bound hM4Di-miniGo, CNO-bound hM3Dq-miniGq, and iperoxo-bound hM3R-miniGq. For each of the respective complexes are shown: **a**, Selected frame aligned micrograph. The experiment was repeated three times with similar results. **b**, Histograms of defocus values for micrographs used in the single-particle analysis (see Extended Data Table 1 for more details). **c**, Orientational distribution heat map. **d**, 2D plots of the gold-standard Fourier shell correlation (GSFSC) between half maps (black) and FSC between model and the b-factor sharpened map for respective refined model (red) as calculated by phenix.mtirage. Local refinement GSFSC is shown in gray and the locally refined map to the model is shown in plumb. **e**, Local resolution heat-map calculated using the local windowed FSC method.

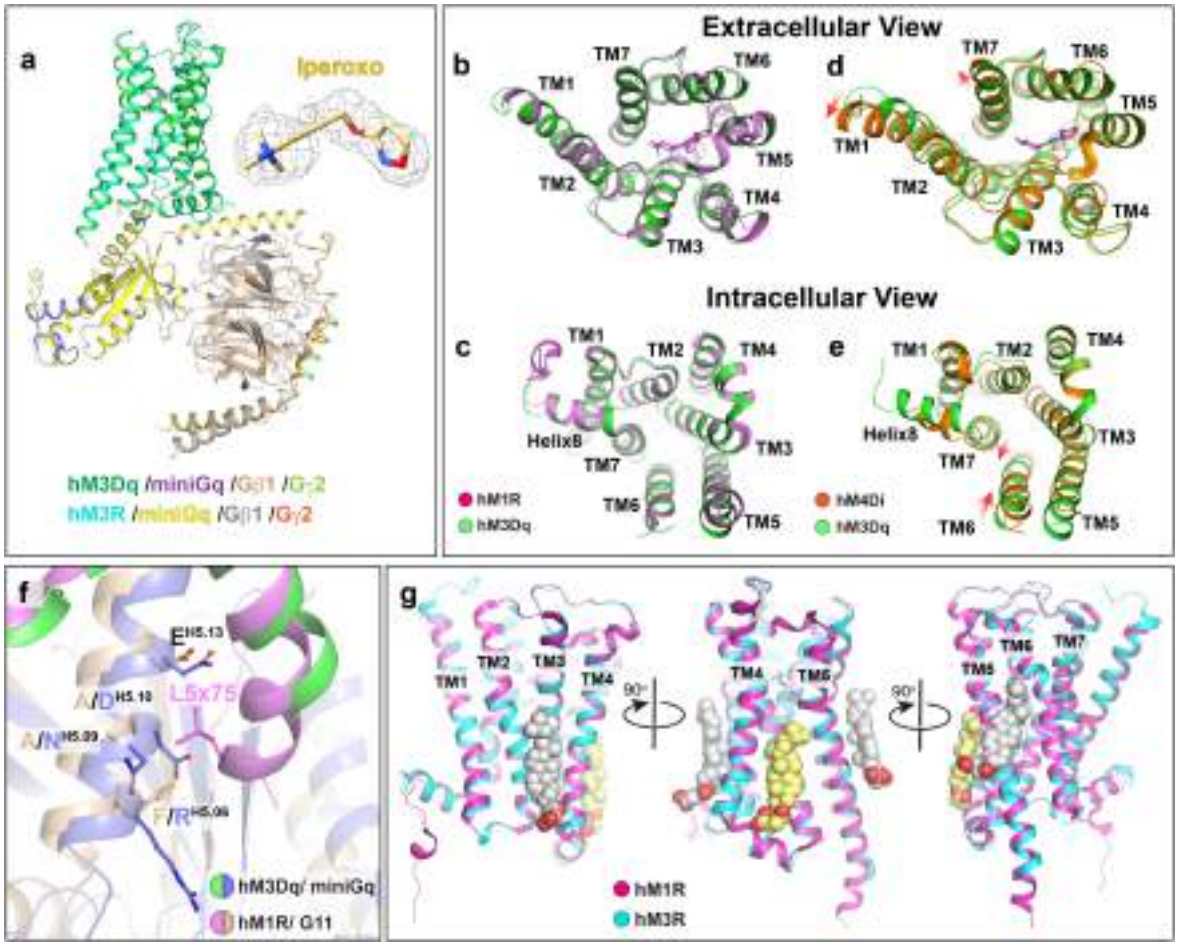

Extended Data Fig. 3 | Overall structure and CHS binding site of the iperoxo bound hM3R-miniGq complex. a, Superposition of the overall structures of the iperoxo-bound hM3R-miniGq and DCZ-bound hM3Dq-miniGq. The density map of the iperoxo is shown as gray meshes. **b**-**c**, The extracellular (**b**) and intracellular (**c**) views of structural comparison of the receptors between hM1R-G_{11} (PDB: 6OIJ) and hM3Dq-miniGq complexes, respectively. **d**-**e**, The extracellular (**d**) and intracellular (**e**) views of structural comparison of the receptors between hM3Dq-miniGq and hM4Di-miniGo complexes, respectively. **f**, Comparison of the interfaces between TM5 of hM1R or hM3Dq and α5 helix of G_{11} or miniGq subunit in the structures of hM1R-G_{11} or hM3Dq-miniGq complex. **g**, Three views of the superposition of hM1R (6OIJ) and hM3R structures. The CHS molecules in the hM1R or hM3R structure are shown in gray or yellow spheres, respectively.

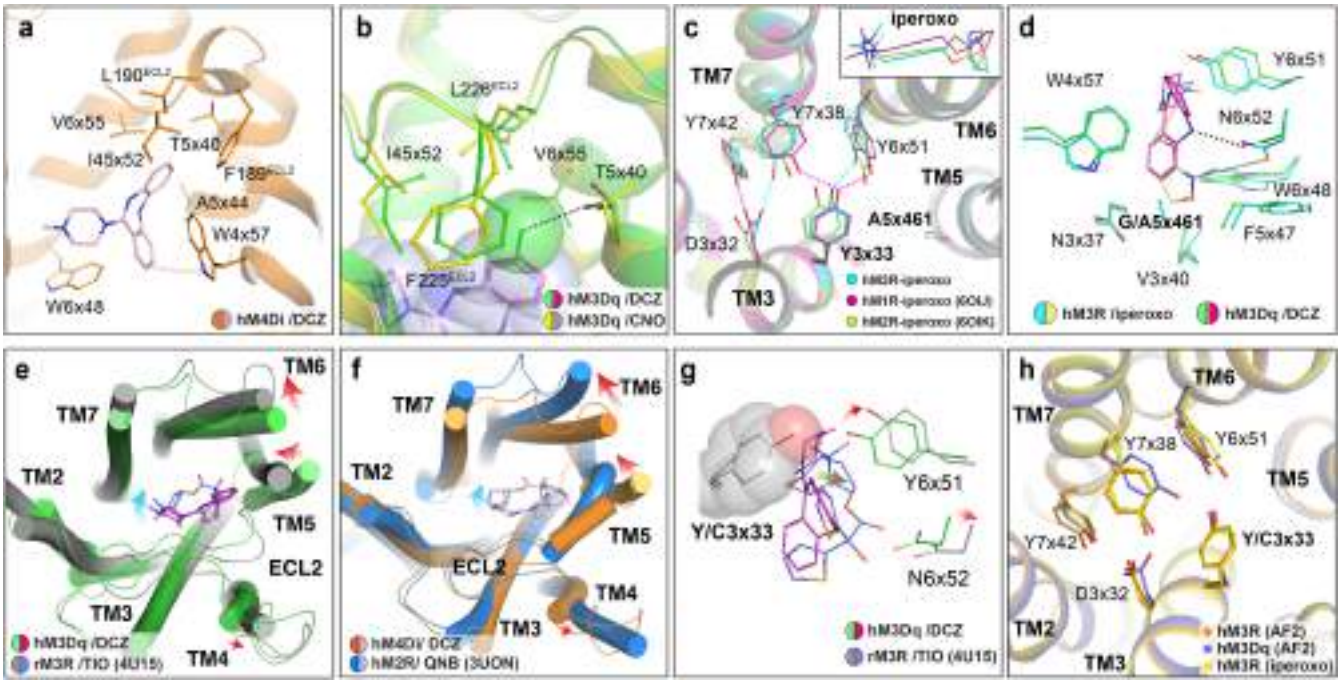

Extended Data Fig. 4 | Ligand binding pockets in DREADD and WT receptors. **a**, Side view of the binding pocket of the hM4Di-DCZ structure. Both DCZ and surrounding residues interacting with DCZ are shown in stick models. **b**, Interactions of the 8-chloro group of CNO with surrounding residues in the CNO-hM3Dq structure. The compound CNO is shown in both stick and sphere models and DCZ and surrounding residues are shown in the ball-and-stick model. **c**, Superposition of the binding pockets of hM3R-iperoxo, hM1R-iperoxo (6OIJ), and hM2R-iperoxo (6OIK) structures. The inset shows the structural comparison of the iperoxo molecules in the binding pockets of these three structures. Hydrogen bonds are indicated as dashed lines. **d**, Side view of the binding pockets of superposed hM3Dq-DCZ and hM3R-iperoxo structures. The deeper subpocket occupied by the heterocyclic group of iperoxo is formed by N3x37, V3x40, F5x47, W6x48, and N6x52. **e**-**f**, Structural comparisons of the hM3Dq-DCZ and rM3R-tiotropium (TIO, 4U15) structures (**e**), and the hM4Di-DCZ and hM2R-QNB (PDB: 3UON) structures (**f**). Major conformational differences of the TM4, TM5, and TM6 on the extracellular side and ligands are indicated by red and blue arrows, respectively. Ligands are shown in stick models. **g**, Interactions between DCZ or TIO and Y/C3x33, Y6x51, and N6x52 in hM3Dq or rM3R structure. The Y3x33 is shown in spheres. The conformational changes of the ligands and residues are indicated by gray and red arrows, respectively. **h**, Top view of the binding pocket comparison of predicted hM3R structure from the alphafold2 (AF2) server, modeled hM3Dq structure by alphafold2 server, and hM3R in the structure of the iperoxo-bound hM3R-miniGq complex.

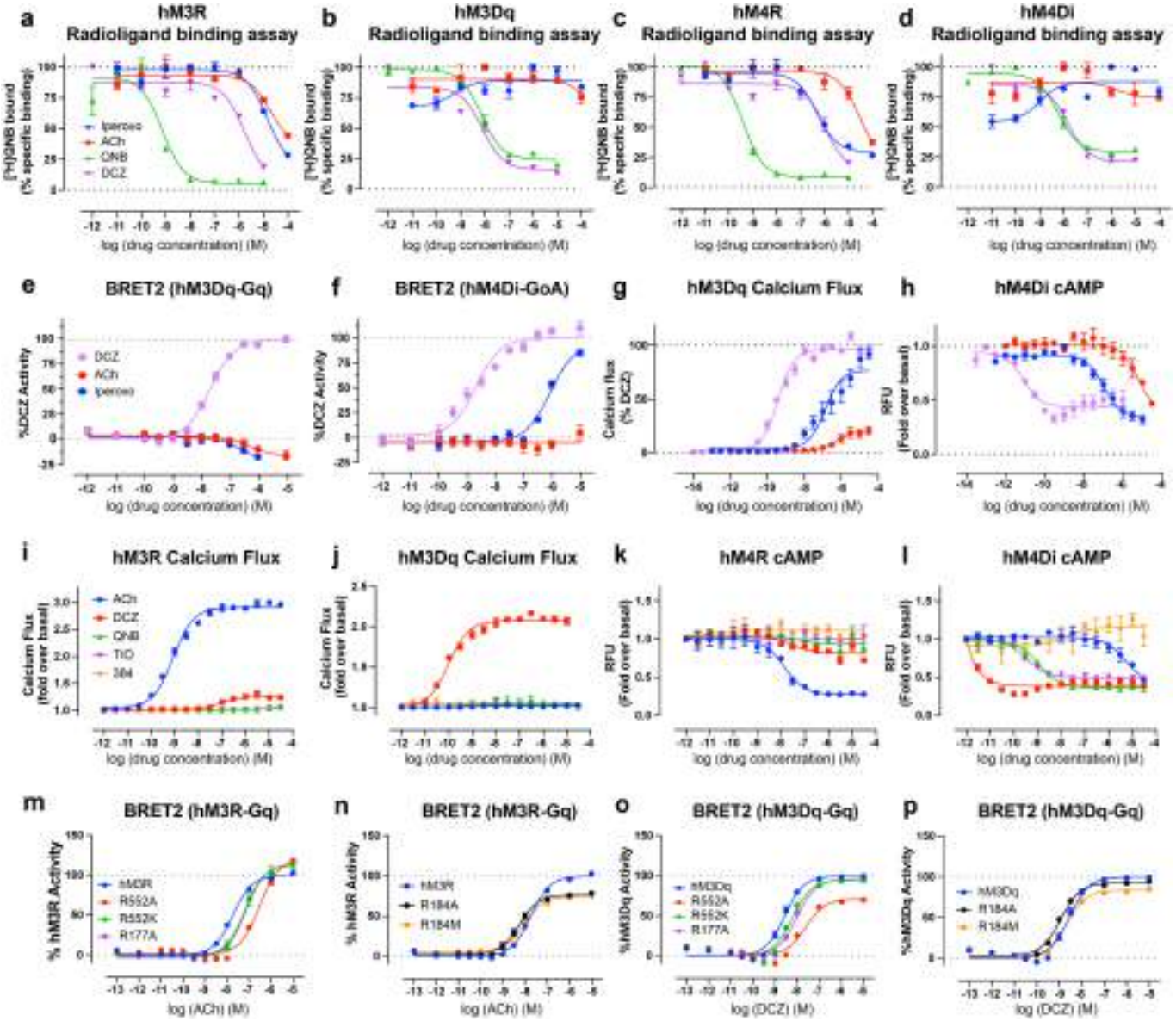

Extended Data Fig. 5 | Functional validations of iperoxo and QNB towards the WT or DREADD receptors. a–**d**, Binding affinities of iperoxo towards the WT and DREADD receptors. See Supplementary Table 5 for fitted parameter values that represent the mean ± SEM of n = 3 biologically independent experiments. **e**-**f**, Iperoxo, ACh, and DCZ agonist activities toward DREADD receptors by BRET2 assay. See Supplementary Table 6 for fitted parameter values that represent the mean ± SEM of n = 4 biologically independent experiments. **g**-**h**, Iperoxo, ACh, and DCZ agonist activities toward DREADD receptors by calcium flux assay (**g**) and cAMP Glo-sensor assay (**h**). See Supplementary Table 7 for fitted parameter values that represent the mean ± SEM of n = 3–5 biologically independent experiments. **i**-**l**, Gq activities of hM3R (**i**) and hM3Dq (**j**) under the stimulation of compounds ACh, DCZ, QNB, TIO, and 384 by FLIPR calcium assay and Gi/o activities of hM4R (**k**) and hM4Di (**l**) under the stimulation of compounds ACh, DCZ, QNB, tiotropium (TIO), AD-DX 384 (384) by split-luciferase-based cAMP Glo-sensor assay. See Supplementary Table 8 for fitted parameter values that represent mean ± SEM of n = 3 biologically independent experiments. **m**-**p**, Mutagenesis analysis of three arginines (R177, R184, and R552) in the ACh-induced activation for hM3R (**m**-**n**) and DCZ-induced activation for hM3Dq (**o**-**p**) by the BRET2 assay, respectively. See Supplementary Table 9 for fitted parameter values that represent mean ± SEM of n = 4 biologically independent experiments.

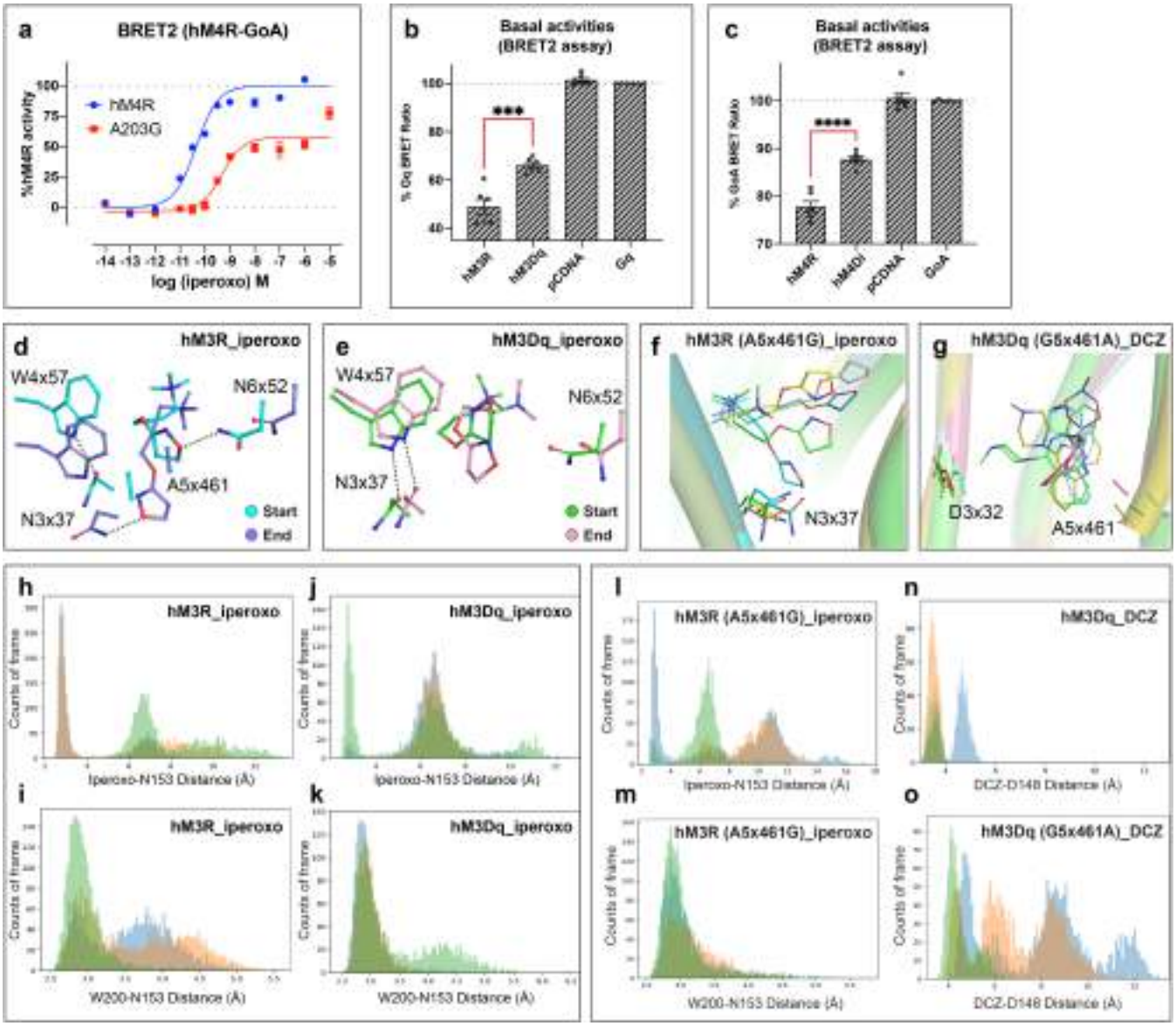

Extended Data Fig. 6 | MD simulations of iperoxo and DCZ in WT and DREADD receptors. a, Activation of hM4R and hM4R (A203G) under the stimulation of iperoxo by the BRET assay. See Supplementary Table 10 for fitted parameter values that represent mean ± SEM of n = 4 biologically independent experiments. **b**-**c**, Basal activities of hM3Dq (**b**) and hM4Di (**c**) by BRET2 assay. Data represent the mean ± SEM. ***p = 0.0004 (hM3Dq, n = 6), ****p < 0.0001 (hM4Di, n = 6), unpaired two-tailed student t-test. **d**-**e**, Interaction between W4x57 and N3x37 at the start and end snapshots of the simulation of hM3Dq-iperoxo (**d**) and hM3R-iperoxo (**e**). **f**-**g**, Representative poses of iperoxo (**f**) and DCZ (**g**) in the hM3R (A5x461G) and hM3Dq (G5x461A) during the MD simulation, respectively. **h**−**m**, Statistics analysis of the iperoxo-N153 distance (isoxazole oxygen of iperoxo to ND2 of N153) and W200-N153 distance (indole N of W200 to OD1 of N153) in the simulation of hM3R-iperoxo (**h** and **i**), hM3Dq-iperoxo (**j** and **k**), and hM3R (A5x461G)-iperoxo (**l** and **m**), respectively. **n**-**o**, Statistics analysis of the DCZ-D148 distance [nitrogen on the piperazine ring (N02) of DCZ to OD2 of D148] in the simulation of hM3Dq-DCZ (**n**) and hM3Dq (G5x461A)-DCZ (**o**), respectively. The x-axis represents the binned distance and the y-axis is the count of frames from the simulations. Each color represents separate runs from the respective simulations.

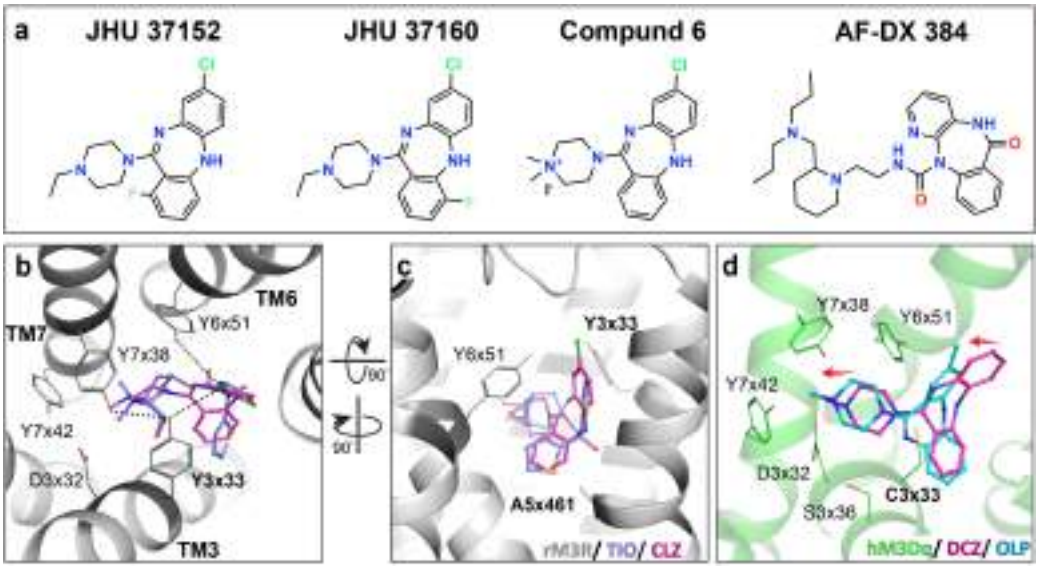

Extended Data Fig. 7 | Docking poses of clozapine in inactive rM3R and olanzapine in hM3Dq structures. a, Chemical structures of JHU 37152 (J52), JHU 37160 (J60), compound 6 from the previous SAR study, and AF-DX 384 (384). **b**-**c**, Two views of the superposition of the preferred docking pose of clozapine (CLZ) and binding pose of tiotropium (TIO) in the inactive state rM3R structure (4DAJ). **d**, Superposition of the preferred docking pose of the olanzapine (OLP) and binding pose of DCZ in the hM3Dq structure. The conformational differences from DCZ to OLP are indicated by red arrows.

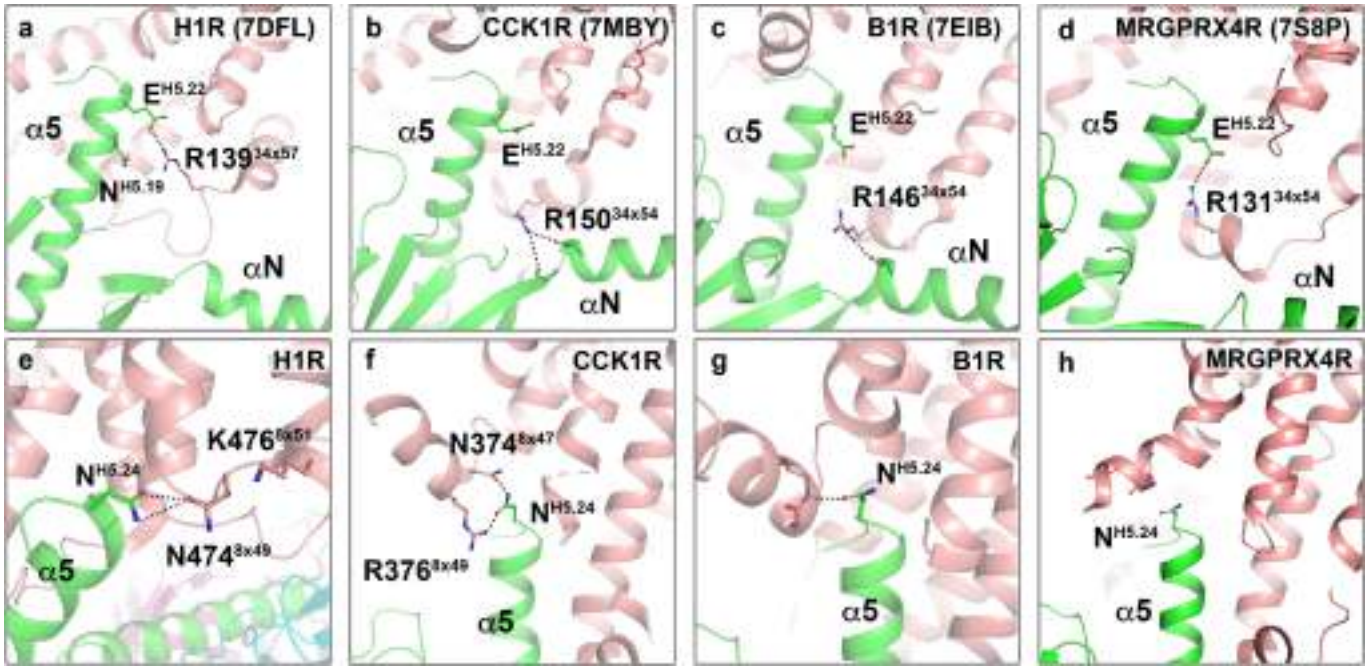

Extended Data Fig. 8 | Receptor-Gq protein interfaces in different complexes. a–**h** Interfaces mediated by the feature residue $E^{H5.22}$ (**a**–**d**) and $N^{H5.24}$ (**e**–**h**) in the Gq protein engaged H1R (**a**, **e**), CCK1R (**b**, **f**), B1R (**c**, **g**), and MRGPRX4R (**d**, **h**) complexes, respectively.

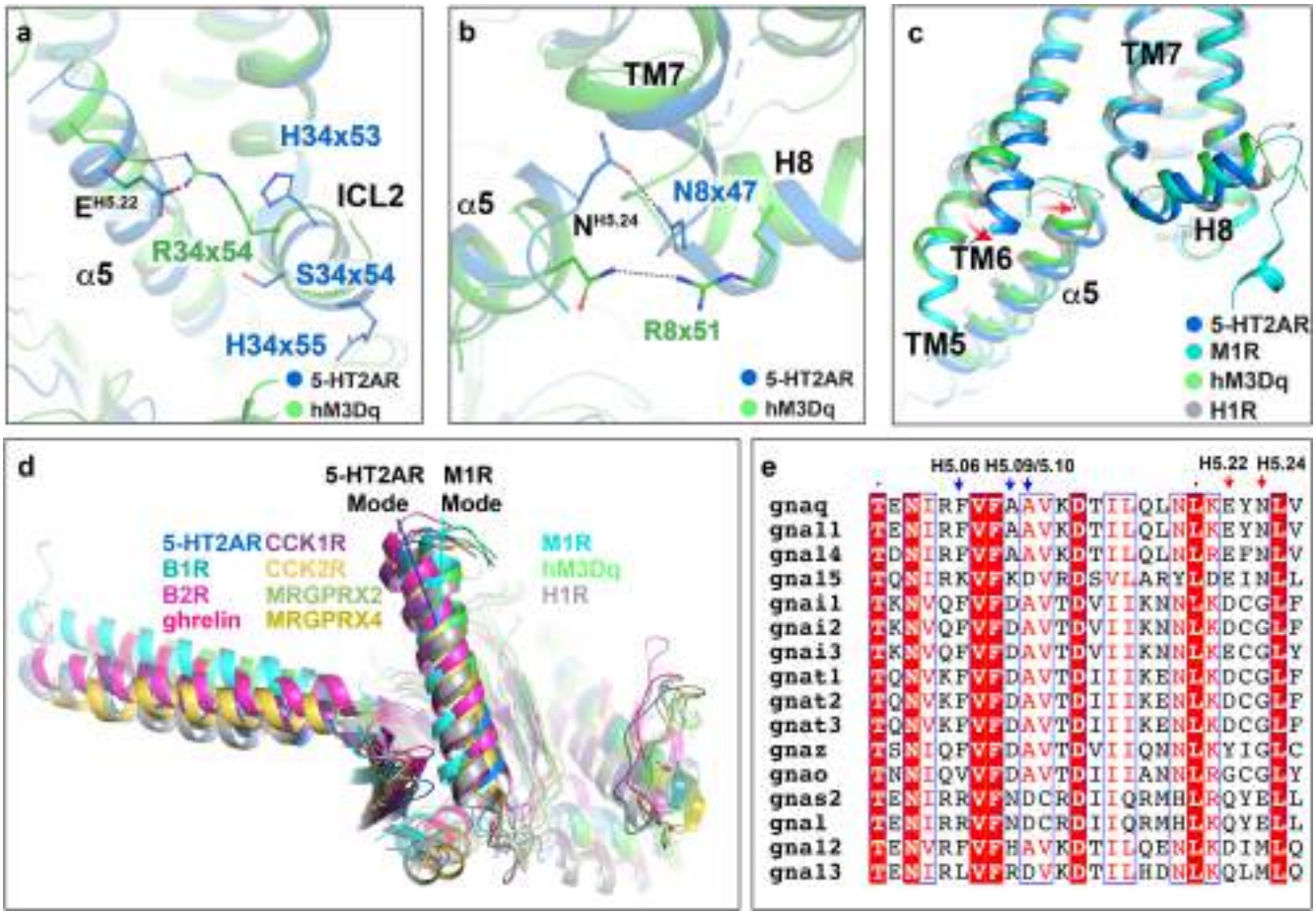

Extended Data Fig. 9 | Two distinct Gq coupling modes. a-b, Comparison of the receptor-G protein interfaces mediated by the $E^{H5.22}$ (**a**) and $N^{H5.24}$ (**b**) in the 5-HT2A-miniGq and hM3Dq-miniGq structures, respectively. **c**, Conformational changes of the TM6 of the receptor and α5 helix of the Gq subunit among the 5-HT_{2A}R-miniGq (6WHA), hM1R-G11 (6OIJ), hM3Dq-miniGq, and H1R-miniGq (7DFL) structures. **d**, Structural comparison of the Gq proteins in the complexes of receptors 5-HT_{2A}R (6WHA), B1R (7EIB), B2R (7F2O), ghrelin receptor (7F9Y), CCK1R (7MBY), CCK2R (7F8W), MRGPRX2 (7S8L), MRGPRX4 (7S8P), hM1R (6OIJ), hM3Dq, and H1R (7DFL). **e**, Sequence alignment of α5 helices of all Gα subunits. Residues involved in the interactions with TM5 of hM1R are indicated by the blue arrows. And two feature residues in $G_{q/11}$ subfamily are indicated by the red arrows.

Extended Data Table 1 | Cryo-EM data collection, refinement and validation statistics

Structures	hM3Dq-miniGq DCZ (PDB: 8E9W) (EMD-27966)	hM4Di-miniGo DCZ (PDB: 8E9X) (EMD-27967)	hM3Dq-miniGq CNO (PDB: 8E9Y) (EMD-27968)	hM3R-miniGq iperoxo (PDB: 8E9Z) (EMD-27969)	hM3R-iperoxo (local refinement) (PDB: 8EA0) (EMD-27970)
Data collection and processing					
Magnification	45,000	45,000	45,000	45,000	
Voltage (kV)	200	200	200	200	
Electron exposure (e–/Å^2)	46.1	46.1	47.0	59.0	
Defocus mean (SD) µm[1]	1.2 (0.3)	1.0 (0.3)	1.2 (0.3)	1.1 (0.3)	
Defocus Range	0.3-3.4	0.2-2.9	0.4-2.8	0.3-2.1	
Pixel size (Å)	0.88	0.88	0.88	0.88	
Symmetry imposed	C1	C1	C1	C1	
Initial particle images (no.)	964,824	731,307	812,816	901,978	
Final particle images (no.)	462,349	435,476	579,660	591,814	
Map resolution (Å)	2.69	2.70	2.79	2.55	2.56
FSC threshold	0.143	0.143	0.143	0.143	0.143
Map resolution range (Å)	2.3-4.3	2.4-4.4	2.4-5.3	2.3-4.7	2.4-3.6
Refinement					
Initial model used (PDB code)	6OIJ	6OIK	8E9W	8E9W	8E9W
Model resolution (Å)[2]	2.92	2.93	3.19	2.95	3.12
FSC threshold	0.5	0.5	0.5	0.5	0.5
Model resolution range (Å)	2.3-4.3	2.4-4.4	2.4-5.3	2.3-4.7	2.4-3.6
Map sharpening B factor (Å^2)	89.7	87.5	86.0	86.6	77.8
Model composition					
Non-hydrogen atoms	8,529	8,380	8,480	8,567	2,286
Protein residues	1,123	1,109	1,123	1,129	285
Ligands	1	1	1	2	2
B factors (Å^2)					
Protein	52.54	50.34	54.08	51.24	42.41
Ligand	55.06	49.30	48.99	59.49	39.74
R.m.s. deviations					
Bond length (Å)	0.003	0.003	0.005	0.005	0.007
Bond angle (°)	0.617	0.544	1.084	0.786	0.470
Validation					
MolProbity score	1.56	1.64	1.97	1.70	1.77
Clash score	7.31	6.28	12.62	9.60	8.88
Poor rotamer (%)	0.11	0.0	0.12	0.34	0.0
Ramachandran Plot					
Favored (%)	97.1	95.8	94.75	96.85	95.73
Allowed (%)	2.9	4.2	5.25	3.15	4.27
Disallowed (%)	0.0	0.0	0.0	0.0	0.0

One underfocus positive, two resolution estimates from cryoSPARC auto-corrected GSFSC.

nature portfolio

Corresponding author(s): Jonathan F. Fay and Bryan L. Roth

Last updated by author(s): Oct 10, 2022

Reporting Summary

Nature Portfolio wishes to improve the reproducibility of the work that we publish. This form provides structure for consistency and transparency in reporting. For further information on Nature Portfolio policies, see our Editorial Policies and the Editorial Policy Checklist.

Statistics

For all statistical analyses, confirm that the following items are present in the figure legend, table legend, main text, or Methods section.

n/a	Confirmed	
☐	☒	The exact sample size (*n*) for each experimental group/condition, given as a discrete number and unit of measurement
☐	☒	A statement on whether measurements were taken from distinct samples or whether the same sample was measured repeatedly
☐	☒	The statistical test(s) used AND whether they are one- or two-sided *Only common tests should be described solely by name; describe more complex techniques in the Methods section.*
☒	☐	A description of all covariates tested
☒	☐	A description of any assumptions or corrections, such as tests of normality and adjustment for multiple comparisons
☐	☒	A full description of the statistical parameters including central tendency (e.g. means) or other basic estimates (e.g. regression coefficient) AND variation (e.g. standard deviation) or associated estimates of uncertainty (e.g. confidence intervals)
☐	☒	For null hypothesis testing, the test statistic (e.g. *F*, *t*, *r*) with confidence intervals, effect sizes, degrees of freedom and *P* value noted *Give P values as exact values whenever suitable.*
☒	☐	For Bayesian analysis, information on the choice of priors and Markov chain Monte Carlo settings
☒	☐	For hierarchical and complex designs, identification of the appropriate level for tests and full reporting of outcomes
☒	☐	Estimates of effect sizes (e.g. Cohen's *d*, Pearson's *r*), indicating how they were calculated

Our web collection on statistics for biologists contains articles on many of the points above.

Software and code

Policy information about availability of computer code

Data collection	SerialEM V3.8.2 (CryoEM)
Data analysis	Structure determination and refinement: cryoSPARC V3.1.0, Topaz 0.2.2, DeepEMhancer, UCSF Chimera 1.15, UCSF ChimeraX 1.3, PyMol 2.4.1, Coot 0.9.5, MolProbity (built in phenix 1.18.2), Phenix 1.18.2 Functional data analysis: GraphPad Prism 9.2 Ligand illustrator: ChemDraw 20.0. Docking and molecular simulation: Maestro v12.9 (Schrodinger v2021-3), CHARMM-GUI (https://www.charmm-gui.org/), AMBER v20.12 (including CUD and PMEMD), Visual Molecular Dynamics (VMD) v1.9.4a48, matplotlib v3.4.3, seaborn v0.11.2, pytraj v2.0.6

For manuscripts utilizing custom algorithms or software that are central to the research but not yet described in published literature, software must be made available to editors and reviewers. We strongly encourage code deposition in a community repository (e.g. GitHub). See the Nature Portfolio guidelines for submitting code & software for further information.

Data

Policy information about availability of data

All manuscripts must include a data availability statement. This statement should provide the following information, where applicable:

- Accession codes, unique identifiers, or web links for publicly available datasets
- A description of any restrictions on data availability
- For clinical datasets or third party data, please ensure that the statement adheres to our policy

The structures of the hM3Dq-miniGq-DCZ, hM4Di-miniGo-DCZ, hM3Dq-miniGq-CNO, hM3R-miniGq-iperoxo, and hM3R-iperoxo (local refinement) have been deposited with the PDB (EMDB) under accession codes 8E9W (EMD-27966), 8E9X (EMD-27967), 8E9Y (EMD-27968), 8E9Z (EMD-27969), and 8EA0 (EMD-27970).

The cryoEM micrographs of hM3Dq-miniGq-DCZ, hM4Di-miniGo-DCZ, hM3Dq-miniGq-CNO, and hM3R-miniGq-iperoxo have been deposited in the EMPIAR database (https://www.ebi.ac.uk/empiar/) with accession numbers EMPIAR-11185, EMPIAR-11184, EMPIAR-11193, and EMPIAR-11194, respectively.

Published PDB files used in this study: hM1R-G11 (6OIJ), hM2R-Go (6OIK), hM2R-QNB (3UON), rM3R-tiotropium (4U15), rM3R-tiotropium (4DAJ), 5-HT1A-Gi (7E2Y), 5-HT2A-miniGq (6WHA), H1R-Gq (7DFL), CCK1R-miniGq (7MBY), CCK2R-Gq (7F8W), B1R-Gq (7EIB), B2R-Gq (7F2O), Ghrelin-Gq (7F9Y), MRGPRX2-miniGq (7S8L), and MRGPRX4-miniGq (7S8P).

Field-specific reporting

Please select the one below that is the best fit for your research. If you are not sure, read the appropriate sections before making your selection.

☒ Life sciences ☐ Behavioural & social sciences ☐ Ecological, evolutionary & environmental sciences

For a reference copy of the document with all sections, see nature.com/documents/nr-reporting-summary-flat.pdf

Life sciences study design

All studies must disclose on these points even when the disclosure is negative.

Sample size	For cryoEM studies, the number of images is determined by the available microscope time and the requirement of the resolution and 3D reconstruction of EM map. For BRET, FLIPR Ca2+ assay, Split-luciferase based cAMP reporter assay, and radioligand binding assays, there is no statistical approached used to predetermine the sample size. For all functional assays, we performed at least three biological replications and this is commonly exploited by the researchers in this field. Exact number of biological replicates are reported in the figure legends.
Data exclusions	No data were excluded.
Replication	For BRET, FLIPR Ca2+ assay, split-luciferase based cAMP reporter assay, and radioligand binding assays, at least three biologically independent experiments (n=3) were performed. Exact number of biological replicates are reported in the figure legends. All the experimental findings were reliably reproduced.
Randomization	No Randomization was attempted as the assays don't have unknown covariates. For example, the comparison between hM4R and mutant hM4R in the signaling studies, there is no feasible unknown covariate that we can minimize by randomizing the experimental groups.
Blinding	No blinding was performed in this study. For both cryoEM structure determination and functional studies, blinding is not necessary due to the nature of these experiments do not requires subject assessment of the data that may influence the validity of the results

Reporting for specific materials, systems and methods

We require information from authors about some types of materials, experimental systems and methods used in many studies. Here, indicate whether each material, system or method listed is relevant to your study. If you are not sure if a list item applies to your research, read the appropriate section before selecting a response.

Materials & experimental systems

n/a	Involved in the study
☐	☒ Antibodies
☐	☒ Eukaryotic cell lines
☒	☐ Palaeontology and archaeology
☒	☐ Animals and other organisms
☒	☐ Human research participants
☒	☐ Clinical data
☒	☐ Dual use research of concern

Methods

n/a	Involved in the study
☒	☐ ChIP-seq
☒	☐ Flow cytometry
☒	☐ MRI-based neuroimaging

Antibodies

Antibodies used	anti-Flag–HRP-conjugated antibody (Sigma-Aldrich, A8592)
Validation	anti-Flag–HRP-conjugated antibody is from mouse clone M2 and used for measuring protein expression on the surface of cells. Detailed information can be found at: https://www.sigmaaldrich.com/US/en/product/sigma/a8592.

Eukaryotic cell lines

Policy information about cell lines

Cell line source(s)	HEK293T cells were purchased from the American Type Culture Collection (ATCC, ATCC CRL-11268). HEK 293 cells were purchased from the American Type Culture Collection (ATCC, CRL 1573). Sf9 cells were obtained from Expression System company (Cat 94-001S)
Authentication	HEK293T and HEK293 cells were authenticated by the supplier (ATCC) using morphology and growth characteristics, and STR profiling. Sf9 cells are commercial and obtained from vendors as indicated in the manuscript. No additional authentication was performed by the authors of this study.
Mycoplasma contamination	HEK293T and HEK293 cells have been tested and shown to be free from mycoplasma (Hoechst DNA strain and Direct Culture methods employed). Sf9 cell line was certified as mycoplasma-free by the source company.
Commonly misidentified lines (See ICLAC register)	None